

## Multispacecraft Measurements in the Magnetosphere

Malcolm W. Dunlop<sup>1,2</sup>, TieYan Wang<sup>2</sup>, XiangCheng Dong<sup>1</sup>, Stein Haarland<sup>3</sup>, QuanQi Shi<sup>4</sup>, HuiShan Fu<sup>1</sup>, Johan De Keyser<sup>5</sup>, Chao Shen<sup>6</sup>, ZhaoJin Rong<sup>7</sup>, Christophe Phillippe Escoubet<sup>8</sup>, ZuYin Pu<sup>9</sup>, and Jonathan Eastwood<sup>2</sup>

## ABSTRACT

This chapter covers a selection of the range of multispacecraft techniques that have been initially developed to analyze Cluster data. We begin the chapter with a short introduction, following this with an account of the methods and their application. The topics are separated into those dealing with magnetic field gradients and topology (which include the curlometer, magnetic rotation analysis, and least squares approach); magnetic field reconstruction and the analysis of magnetic field nulls (which are significant for magnetic reconnection and other geometries); time series analysis, adapted for multispacecraft data (including boundary identification, dimensional, and motion analysis); and wave vector analysis methods in the Fourier domain.

## 40.1. INTRODUCTION

In February 2000, the four Cluster spacecraft began full science operations in eccentric polar orbits (Escoubet et al., 2001). This launch heralded the first time a coordinated array of measurements in space could

be made and allowed spatial gradients of key quantities to be made in a step change for the capacity of magnetospheric measurements. Cluster has maintained a closed array configuration for much of its operating life and remains the only space physics mission to do this with fully four-point coverage of such a large range of spatial scales. During the first several years of its operations the four spacecraft were placed into configurations with spatial scales varying between a few hundred and 2,000 km (Figure 40.1). For this phase of the mission, the spacecraft were maintained in a close array, which achieved a regular configuration at some point on the orbit. Subsequently, more complex operations were achieved in which two spacecraft had much smaller separation distances (left-hand side of Figure 40.1). But throughout its mission all spacecraft have flown in formation throughout the mid to outer magnetosphere, magnetosheath, bow shock, and upstream solar wind. The right-hand side of Figure 40.1 shows that on the dayside the orbit began as a polar asymmetric orbit ( $4 \times 19.6 R_E$ ), but later correction maneuvers resulted in the orbit inclination rolling over and changing apogee height and

<sup>1</sup>School of Space and Environment, Beihang University, Beijing, China

<sup>2</sup>Rutherford Appleton Laboratory, Didcot, Oxfordshire, UK

<sup>3</sup>Birkeland Centre for Space Science, University of Bergen, Bergen, Norway

<sup>4</sup>Institute of Space Sciences, Shandong University, Weihai, China

<sup>5</sup>Royal Belgian Institute for Space Aeronomy, Brussels, Belgium

<sup>6</sup>Harbin Institute of Technology, Shenzhen, China

<sup>7</sup>Institute of Geology and Geophysics, Chinese Academy of Sciences, Beijing, China

<sup>8</sup>European Space Agency/European Space Research and Technology Centre, Noordwijk, The Netherlands

<sup>9</sup>School of Earth and Space Sciences, Peking University, Beijing, China

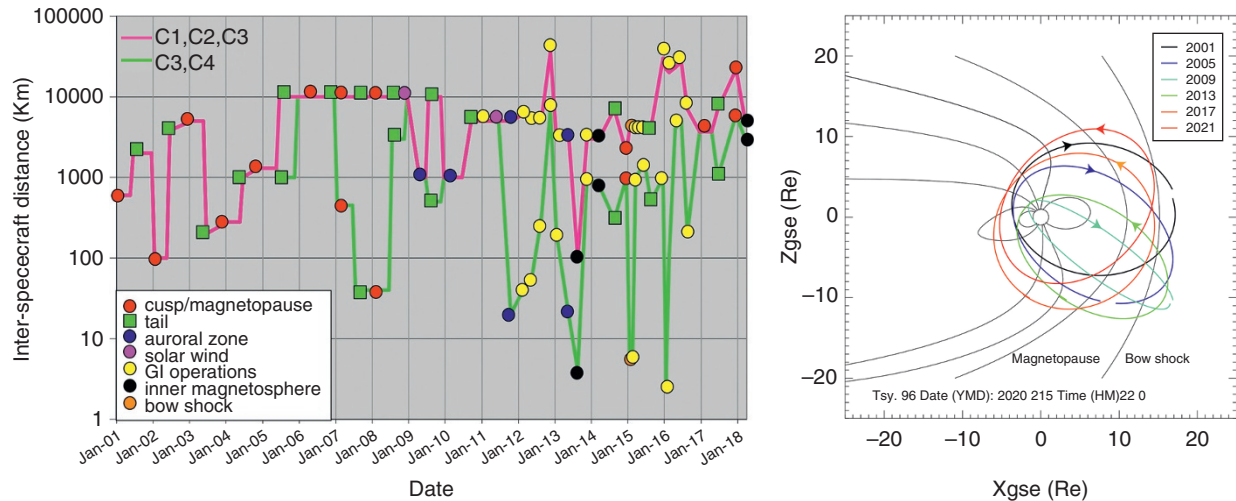


**Figure 40.1** Dayside Cluster orbit evolution and configuration strategy.

position. Currently, Cluster is entering its twenty-first year of full science operations.

As a result of this unprecedented data coverage of the magnetosphere, a wide range of techniques have been developed and applied in different ways to investigate a large number of phenomena and determine key quantities. These techniques have been documented in two ISSI books (Paschmann and Daly, 1998, 2008), together with a range of reviews on their application to key topics (Chanteur, 1998; Dunlop and Eastwood, 2008; Harvey, 1998; Robert et al., 1998; Vogt et al., 2008). Here we pick up the state of the art of these methods and their use, mentioning, in particular, their adaptation to other recent missions (notably MMS, THEMIS and Swarm). The Magnetospheric Multi-Scale (MMS) mission is particularly notable since it follows Cluster in maintaining a close configuration for much of its orbit (Burch et al., 2016), but on much smaller separation scales, while THEMIS has achieved a three-spacecraft configuration (of the magnetospheric spacecraft) in its extended operations (Angelopoulos, 2008), and Swarm achieved smaller two and three spacecraft formations at LEO polar altitudes (Friis-Christensen et al., 2008).

## 40.2. MAGNETIC FIELD GRADIENTS AND TOPOLOGY

### 40.2.1. The Curlometer and Other Spatial Gradient Methods

Magnetic field measurements on board multiple spacecraft flying in formation allow both the gradient and curvature terms in the dyadic of the magnetic field,  $\mathbf{B}$ , to be linearly estimated (Chanteur, 1998; Harvey, 1998; Vogt et al., 2008; Shen and Dunlop, 2008). A full set of gradient

terms can be obtained with an array of at least four spacecraft. Key formulations of this methodology are magnetic rotation analysis (Shen et al., 2007, 2012) and least squares analysis applied to planar reciprocal vectors (De Keyser et al., 2007; Hamrin et al., 2008; Vogt et al., 2009, 2013). The performance of the methods, in general, depends on the integrity of the spacecraft array and the stationary properties (temporal dependence) of the magnetic structures.

In particular, a linear estimate of Ampère's law can be given, i.e. the electric current density from  $\text{curl}(\mathbf{B})$ , in regions where the displacement current ( $\mu_0 \epsilon_0 \partial \mathbf{E} / \partial t$ ) can be neglected (Russell, et al., 2016), where  $\mathbf{B}$  and  $\mathbf{E}$  are the magnetic and electric fields. This method, the curlometer technique (Dunlop et al., 1988, 2016, 2018; Robert et al., 1998; Dunlop and Eastwood, 2008), gives a 3-D vector estimate of current density for a configuration of four spacecraft (i.e.  $\mu_0 < \mathbf{J} > \cdot (\Delta \mathbf{R}_i \Delta \mathbf{R}_j) = \Delta \mathbf{B}_i \cdot \Delta \mathbf{R}_j - \Delta \mathbf{B}_j \cdot \Delta \mathbf{R}_i$ , where  $\Delta \mathbf{B}_i$ ,  $\Delta \mathbf{R}_i$  are the differences in the measured magnetic field and positions to a reference spacecraft). The method is perhaps the most widely used in the magnetosphere (notably applied in: the magnetopause boundary layer (Dunlop et al., 2002a, 2005; Haaland et al., 2004a; Panov et al., 2006); the magnetotail (Runov et al., 2006; Nakamura et al., 2008; Narita et al., 2013); the ring current (Vallat et al., 2005; Zhang et al., 2011; Shen et al., 2014, Yang et al., 2016); field-aligned currents (FACs) (Forsyth et al., 2008; Marchaudon, 2009; Shi et al., 2010, 2011; Ritter et al., 2013; Dunlop et al., 2015a, 2015b); and other transient signatures and in the solar wind (Roux et al., 2015; Xiao et al., 2004; Shen and Dunlop, 2008; Eastwood et al., 2002)). Although robust, errors in the estimate arise from uncertainties in the magnetic field measurements, timing, and the spacecraft separation distances; as well as from the form (scale-size) of the current structure (the neglect

of nonlinear gradients in the calculation). For Cluster separations, typically, the dominant error is that arising from nonlinear gradients. The linear estimator  $Q = |\text{div}\mathbf{B}| / |\text{curl}(\mathbf{B})|$ , is useful as an indirect quality parameter and has been used extensively during Cluster studies. For MMS, measurement errors are more critical, since the currents are usually well resolved on smaller scales, with the result that generally, for MMS, there is a threshold current density magnitude below which the errors affect the estimate (Dunlop et al., 2018). Other spacecraft configurations, such as the array of the three magnetospheric THEMIS spacecraft, or irregular spacecraft separations, can return at least the current density component normal to the plane of the array; useful when the large-scale current orientation is known, as in the case of the ring current, or field-aligned currents (FACs). Where other assumptions in the behavior of the currents can be made (e.g. the stationarity of the magnetic field, or force free structures) the method can be generalized to extend the multipoint sampling (Ritter et al., 2013; Dunlop et al., 2015a).

The standard application of the curlometer since the launch of Cluster was reviewed in Dunlop and Eastwood (2008) and Dunlop et al. (2016, 2018). Ready to use implementations of the method can be obtained from the Cluster Science archive (<http://www.cosmos.esa.int/web/csa/software>); also see the technical note by Middleton and Masson (2016). To highlight the method, Figure 40.2 shows its application to MMS data at the magnetopause (after Dunlop et al., 2018). The plot illustrates that the curlometer estimate closely follows that estimated from the plasma moments ( $\mathbf{J} = \sum \mathbf{qn}_s \mathbf{V}_s \sim \mathbf{qn} (\mathbf{V}_i - \mathbf{V}_e)$ ), averaged over the four spacecraft positions. The individual plasma current estimated at each spacecraft varies significantly however, implying small-scale (filamentary) structure within the magnetopause layer exists, consistent with the details in the current density profile. Such small-scale current density structure, together with large currents, appears to be typical of the magnetopause layer (Dong et al., 2018) and was not seen by Cluster on larger separation scales.

#### 40.2.2. MRA Applications

Based on Cluster's multipoint observations on magnetic field, the methods of curvature analysis (MCA) (Shen et al., 2003) and magnetic rotation analysis (MRA) (Shen et al., 2007) have been developed. By using these methods, the 3-D topology of magnetic field can be deduced, including the curvature radius, normal direction and binormal direction of the magnetic field lines, and, additionally, the rotational features of the magnetic structure. Such analysis uncovered the true 3-D topological structure of the magnetic field in geomagnetosphere for

the first time. As well as the regions mentioned above, the method has been applied to the magnetotail current sheet (Shen et al., 2008a; 2008b; Rong et al., 2011), flux ropes or plasmoids (Zhang et al., 2013; Yang et al., 2014), reconnection regions (Lavraud et al., 2016; Zhang et al., 2016), and the cusp and magnetopause (Shen et al., 2011; Xiao et al., 2018). These results have advanced our understanding of the magnetosphere.

To illustrate the use of the magnetic curvature analysis (MRA), the right-hand side of Figure 40.2 shows estimates of the field-line curvature in the ring current, which shows that the associated implied current density grows with geomagnetic activity (SYM-H) and that the dawn-side crossings are slightly more intense than on the dusk-side. Taking the magnetotail current sheet as another example, we have found the tail current sheet can be divided into three types (the normal, the flattened, and the tilted) based on the yielded field topology. The illustrated cartoons of the three types of current sheet are shown in Figure 40.3.

#### 40.2.3. Least-Squares Methods for Multipoint Gradient Computation

Gradient computation based on four noncoplanar in situ measurements suffers from a number of difficulties. First, it requires exactly four points: with less, the method requires modification; with more, the method is not able to use all the available information. Second, it is based on the assumption that the gradient does not change over the spatial scale corresponding to the separation of the points (the "homogeneity condition"). Third, gradient computation is a difference operator that leads to large relative errors on the result, and this is especially true when the measurements are made close together to satisfy the homogeneity condition.

In many situations (for instance, with Cluster) the instruments record multiple data points in the time span needed for the spacecraft to cover a distance comparable to the typical separation scales. It is then intuitively clear that all those measurements carry information that may be relevant for the calculation of the gradient, as was already noted by Harvey (1998). This is particularly evident if one assumes a certain degree of invariance of the structures of interest as a function of time. This is the idea behind the Gradient Analysis by Least-Squares (GALS) technique (Hamrin et al., 2008).

The Least-Squares Gradient Calculation (LSGC) technique (De Keyser et al., 2007) approximates the quantity to be measured (scalar or vector) with a Taylor series expansion around the point of reference in space and time (typically the barycenter of the set of measurement points). The expansion describes the field in terms of the value at the reference point, its space and time

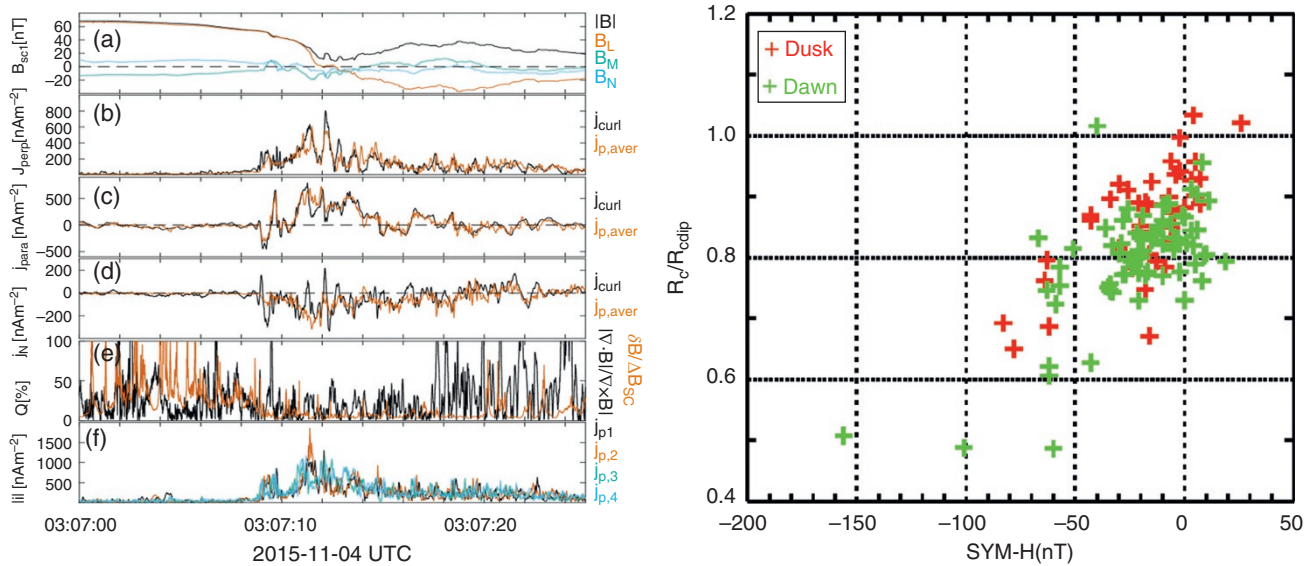


**Figure 40.2** Left: a typical MP crossing seen by MMS for a thickness of  $\sim 350$  km, showing (a) magnetic field in boundary normal coordinates, (b)–(d) the total current density from the curlometer and the mean value of the current density from the four spacecraft ion moments for the perpendicular, parallel, and boundary normal components, (e) comparison of the quality parameter  $Q$  and a crude (upper) estimate of the limit on measurement errors from  $\delta B/\Delta B$ , (f) the individual total current estimated at each spacecraft from the plasma moments. Right: the minimum field-line curvature relative to the curvature of the model dipole field for a set of ring current crossings sampled by Cluster, expressed as the radius of curvature ( $R_C$ ). The crossings are color coded according to dusk and dawn locations in local time. Adapted from Shen et al. (2014).

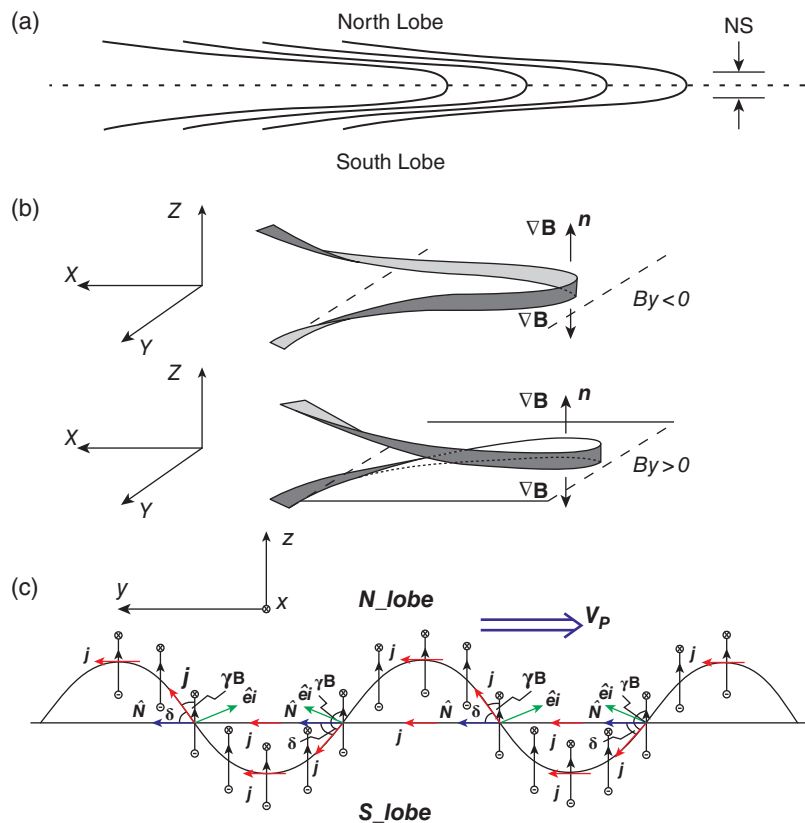


**Figure 40.3** Cartoon of the field topology in: (a) a normal current sheet, (b) a flattened current sheet, and (c) a tilted current sheet. In a normal current sheet, the normal of current sheet is along the  $Z$ -direction and the magnetic field lines are basically in a same plane. In a flattened current sheet, the magnetic field is spiral-like, which is associated with a strong  $B_y$  field component. In the tilted current sheet, the normal of the current sheet deviates strongly from the  $Z$ -axis, induced by flapping motion of the current sheet.

gradients, and higher order nonlinear terms. In the basic version of the method, it is assumed that the homogeneity scales in space and time are known (i.e. the scales over which the gradient can be considered constant) so that the higher order terms can be estimated. Truncating the Taylor expansion after the linear term, one then obtains a linear equation for each available data point. Each of these equations is given a weight based on the measurement and the truncation errors. The resulting overdetermined system is then solved in a weighted least-squares sense, providing the quantity's value and space and time gradients at the point of reference, as well as an error estimate on these results. This error reflects both the measurement errors and the errors that stem from the nonlinear behavior of the gradients. The procedure is repeated along the orbit of the spacecraft formation. In a further development, heuristic techniques have been devised to automatically estimate the homogeneity scales, which makes the method much more convenient (De Keyser, 2008).

Such least-squares methods allow the exploitation of the information content of a larger number of data points and will thus lead to more precise gradient values; in addition, LSGC provides a full error estimate. In many practical situations there is a certain degree of redundancy in the consecutive measurements, so that the increase in precision is real but not necessarily dramatic – it depends on how the space and time sampling scales compare with the homogeneity scales. LSGC allows constraints to be taken into account (e.g. gradient along the magnetic field is zero,  $\text{div}\mathbf{B}=0$ , assuming that the structures are static but not stationary). Adding such constraints strongly improves both the gradient computation itself and the automatic estimation of the homogeneity scales. As a consequence, these techniques can in principle be applied to measurements provided by an arbitrary number of spacecraft, although in practice the quality of the results depends on the measurement errors, the spacecraft orbits and separations, the sampling rate, and the homogeneity scales, but less than the 4-point techniques.

Figure 40.4 illustrates an application of LSGC and highlights how the computation provides error estimates. Although promising, the least-squares gradient methods have not (yet) become main stream because they are computer intensive and not trivial to implement.

### 40.3. MAGNETIC FIELD RECONSTRUCTION AND NULL FIELDS

#### 40.3.1. Magnetic Nulls and the FOTE Method

Another technique focusing on the magnetic field structure is the identification of magnetic nulls and reconstruction of magnetic topology. One such technique, based on

linear variation of the magnetic field around spacecraft tetrahedron, is termed the First-Order Taylor Expansion (FOTE) (Fu et al., 2015, 2020). It operates as a “search-light” on the trajectory of the spacecraft and can resolve the position of magnetic null nearest to the spacecraft tetrahedron. Unlike the Poincare-index method (Xiao et al., 2006), which can only distinguish whether a magnetic null is inside or outside the tetrahedron, this technique can find a magnetic null both inside and outside the tetrahedron and also deduce its drift velocity (Fu et al., 2015, 2018). Such technique has been tested using the 3-D particle-in-cell simulation data (Fu et al., 2015) and has been successfully applied to both the Cluster (Fu et al., 2016, 2017; Wang et al., 2017; Chen et al., 2018a; Liu et al., 2018) and MMS (Fu et al., 2018; Chen et al., 2018b; Man et al., 2018; Huang et al., 2018; Liu et al., 2019) data to resolve structures in the Earth's magnetosphere. According to the test (Fu et al., 2015), such a technique is empirically accurate when a magnetic null is resolved within one ion inertial length near the spacecraft tetrahedron. It will not be affected by the data resolution, instrumental offset, and tetrahedron size (Fu et al., 2015). It is particularly useful to the study of magnetic null and magnetic islands (flux ropes), which have been suggested in previous studies as linear structures (Parnell et al., 1996). Figure 40.5 is an example demonstrating the application of the FOTE technique to a spiral magnetic null around the Cluster spacecraft on 2 October 2003. Specifically, Figures 40.5a–40.5f (left-hand column) demonstrate the application of FOTE to find a spiral null, while Figures 40.5g–40.5h (right-hand column) demonstrate the application of FOTE to reconstruct the topology of this null. In Figures 40.5a–40.5d, the magnetic field strength and three components (L, M, N) are shown. In Figure 40.5e, the minimum distance between magnetic null and each of the four Cluster spacecraft, with null types labelled, is shown. In Figure 40.5f, the two parameters,  $\eta \equiv |\nabla \cdot \mathbf{B}|/|\nabla \times \mathbf{B}|$  and  $\xi \equiv |(\lambda_1 + \lambda_2 + \lambda_3)|/|\lambda|_{\max}$ , for quantifying the quality of the FOTE results (Fu et al., 2015), are shown. And in Figures 40.5g–40.5h, the 3-D topology of the spiral null and the 2-D view of this topology are shown.

The null types in Figure 40.5e are identified based on the Jacobian matrix  $\delta\mathbf{B}$  of the magnetic field around the null. The Jacobian matrix has three eigenvectors,  $\mathbf{v}_1$ ,  $\mathbf{v}_2$ ,  $\mathbf{v}_3$ , and correspondingly has three eigenvalues,  $\lambda_1$ ,  $\lambda_2$ ,  $\lambda_3$ . The sum of these three eigenvalues is zero ( $\lambda_1 + \lambda_2 + \lambda_3 \equiv \nabla \cdot \mathbf{B} = 0$ ), because the magnetic field is “nondivergent” (Dunlop et al., 2002a). This implies that either all the eigenvalues are real or one is real while the two others are conjugate complex (Lau and Finn, 1990). If all the eigenvalues are real, the null is of radial type, which includes both A- and B-type. The A null has one positive and two negative eigenvalues, while the B null has two

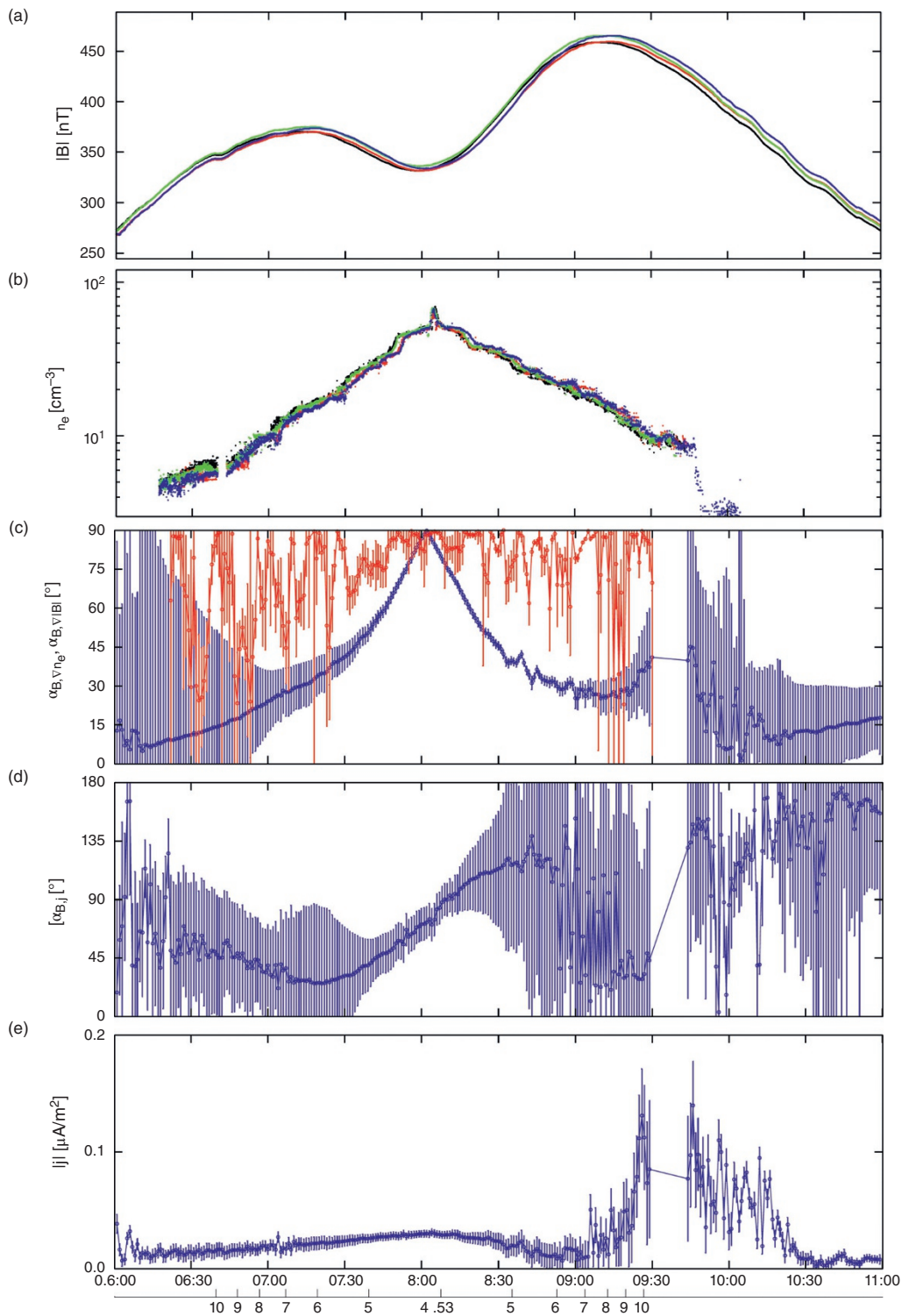


**Figure 40.4** Orientation of gradients during the Cluster inner magnetosphere pass on 7 August 2003, as a function of time (in UT) and of  $L$ -shell of the barycenter of the satellite tetrahedron (bottom scale). The spacecraft separations were  $200 \times 400 \times 1000$  km in the GSE  $X, Y, Z$  directions near perigee around 08:02 UT. All error bars account for measurement errors and nonlinear gradient effects. (a) Magnetic field strength  $|\mathbf{B}|$ . (b) Electron density  $n_e$  identified from the plasma frequency (C1 – black, C2 – red, C3 – green, C4 – blue). (c) Angle  $\alpha_{\mathbf{B}, \nabla|\mathbf{B}|}$  and  $\alpha_{\mathbf{B}, \nabla n_e}$  between the magnetic field and the gradient of the field strength (blue) and between the magnetic field and the electron density gradient (red); the angles are  $90^\circ$  around the equator near perigee. (d) Angle  $\alpha_{\mathbf{B}, \mathbf{j}}$  between the field and the current density  $\mathbf{j} = \nabla \times \mathbf{B}/\mu_0$ . (e) Current density magnitude  $|\mathbf{j}|$ , significantly nonzero in the plasmasphere, indicating deviations from a dipolar field. Figure adapted from De Keyser et al. (2007); Licensed under CC BY 3.0.

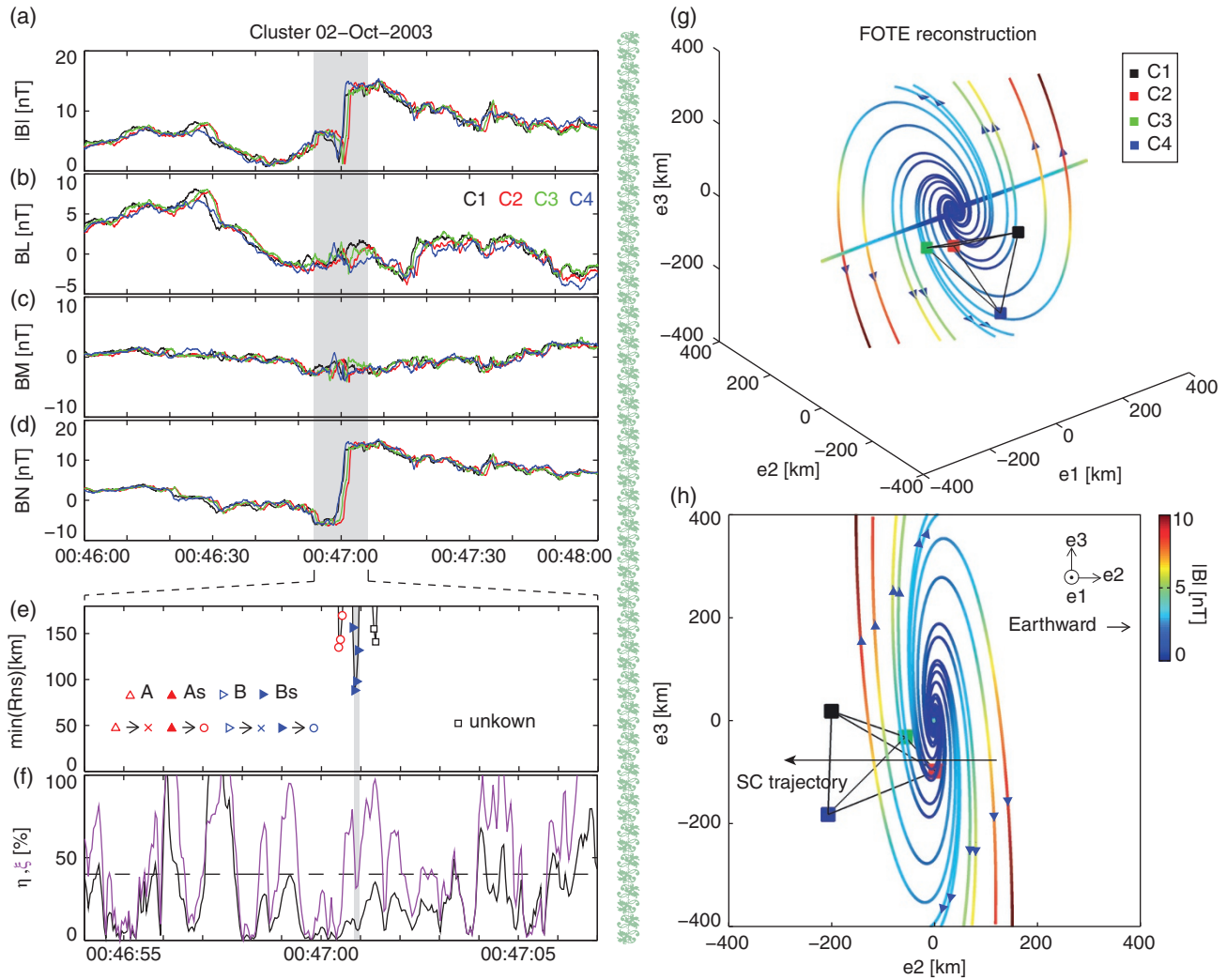


**Figure 40.5** An example demonstrating the application of the FOTE technique to a spiral null around the Cluster spacecraft on 2 October 2003. Specifically, the left-hand column demonstrates the application of FOTE to find a spiral null, while the right-hand column demonstrates the application of FOTE to reconstruct the null topology. Adapted from Fu et al. (2016).

positive and one negative eigenvalues. If one eigenvalue is real while the two others are conjugate complex, the null is of spiral type, which includes  $A_s$ - and  $B_s$ -type. The  $A_s$  null has a positive real eigenvalue, while the  $B_s$  null has a negative real eigenvalue. Regarding the radial null, if one of the eigenvalues is zero, the topology will degenerate to a two-dimensional structure, and correspondingly the A and B nulls degenerate to an X null. Regarding the spiral null, if the real part of the eigenvalues is zero, the topology will also become two-dimensional, and similarly the  $A_s$  and  $B_s$  nulls become an O null. This simplification, from A and B to X, and from  $A_s$  and  $B_s$  to O, is only possible in theory or mathematics, but not in nature or physics, because in nature the eigenvalue never becomes zero, due to the uncertainty of

instrument measurements. Instead, in nature, we can treat one of the eigenvalues as “zero” if it is significantly smaller than the other two eigenvalues. Specifically, following Fu et al. (2015), we may simplify A and B nulls to X null if the three eigenvalues satisfy  $\min(|\lambda|) < \frac{1}{4} \cdot \max(|\lambda|)$  and simplify  $A_s$  and  $B_s$  nulls to O null if the real and imaginary parts of the three eigenvalues satisfy  $\max(|\text{Real}(\lambda)|) < \frac{1}{4} \cdot \min(|\text{Imag}(\lambda)|)$ . In other words, the three-dimensional topology will have a two-dimensional appearance if one of the eigenvalues is very small. If the relation among the three eigenvalues ( $\lambda_1, \lambda_2, \lambda_3$ ) belongs to none of the above categories, due to large uncertainties of instruments or nonlinearity of the magnetic field around magnetic null, we cannot identify the null type and therefore label it as “unknown”.

As can be seen, a spiral null is detected around the Cluster tetrahedron (Figure 40.5e), with the minimum null-SC distance less than 100 km. This null belongs to  $B_s$  type. It should be accurately resolved, because during the detection of the null the two parameters are small ( $\eta < 40\%$  and  $\xi < 40\%$ ). The topology of this null exhibits a very nice spiral feature (Figure 40.5g), with the spine primarily along the  $e_1$  direction and the fan in the  $e_2e_3$  plane. Looking along the  $-e_1$  direction (Figure 40.5h), the topology shows a magnetic island (or flux rope) feature. In the fan plane, the magnetic field is diverging (Figure 40.5g), consistent with definition of the  $B_s$ -type null (Lau and Finn, 1990). Since this technique (FOTE) does not assume the structure to be time-stationary, it can also resolve the temporal evolution of a magnetic structure in space.

### 40.3.2. Magnetic Field Reconstruction

As described above, null points are places where magnetic field vanishes. In magnetospheric plasmas, reconnection configurations with nulls in two-dimensional (2-D) geometry, that is, X-points have been proposed and studied widely. However, for an arbitrary interplanetary magnetic field orientation, reconnection is predicted to occur along a field line linking a pair of nulls (converges A type and diverges B type) in three-dimensional (3-D) geometry, known as the separator, and separatrix surfaces, known as  $\Sigma$ -surfaces or preferably fans (Priest and Titov, 1996), generated by the nulls (Lau and Finn, 1990). On the other hand, nulls and their 3-D properties are also of crucial importance in topology, nonlinear

dynamics, and the interaction of complex fields (Wang and Bhattacharjee, 1996).

Xiao et al. (2006) used data from four Cluster constellation spacecraft to identify positively the presence and structure of an isolated null point in the magnetotail. The simultaneous collection of data from the four separated spacecraft enables its presence to be inferred by calculation of the Poincaré index or topological degree (Greene, 1992) of the surrounding magnetic field. The Poincaré index calculated from these data jumped from 0 to +1 and back again, indicating the occurrence of a null within the tetrahedron defined by the four spacecraft, the first such identification. Following this, a pair of nulls, the null-null line that connects them, and associated fans and spines in the magnetotail are identified also by using four Cluster spacecraft data (Xiao et al., 2007).

To clarify the magnetic topologic property of 3-D MR process, He et al. (2008a, 2008b) reconstructed the magnetic field by using a fitting-reconstructing technique, which is based on a model containing two main constituents of the magnetic field in the magnetotail: a potential field and a Harris current sheet (Harris, 1962). Using the magnetic field vectors instantaneously measured at four positions by FGM on board Cluster, the 12 unknown parameters in 12 equations which constitute the fitting model can be calculated. Then the magnetic field around the Cluster spacecraft is derived (more details see He et al., 2008a). Using this method, separator magnetic reconnection configuration has also been confirmed at dayside magnetopause (Figure 40.6a) (Dunlop et al., 2009) and magnetotail with both antiparallel and component

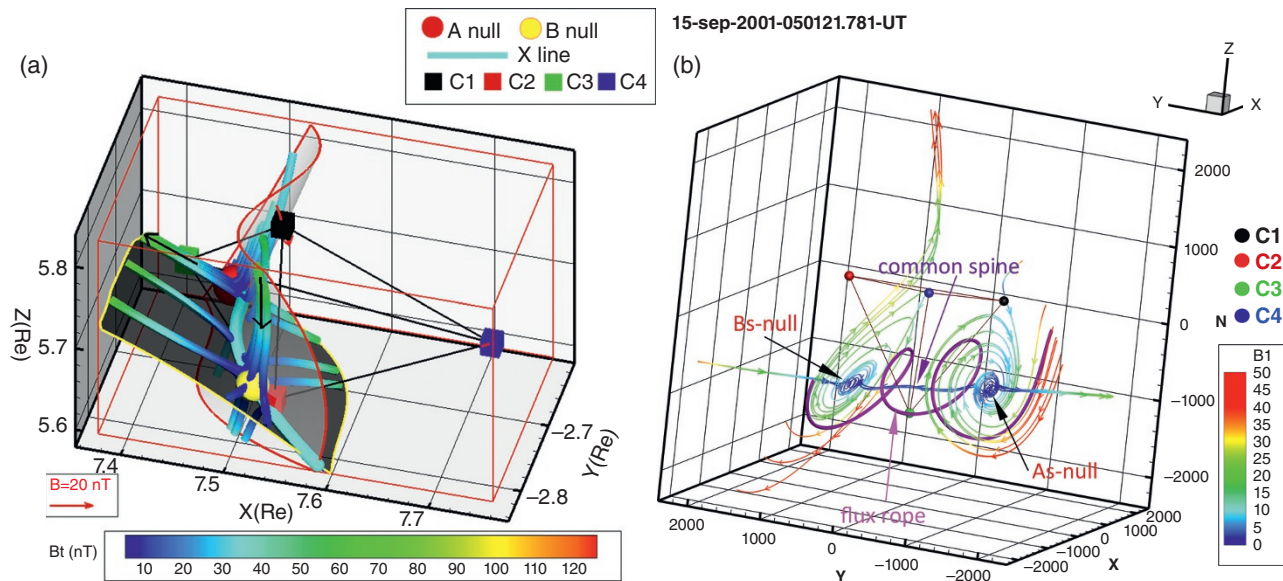


**Figure 40.6** Magnetic field reconstruction results for (a) a magnetopause reconnection and (b) a flux rope event. Both of them have a separator connecting a pair of A-B null points.

reconnection (Guo et al., 2013). Furthermore, flux ropes formed association with a pair of spiral nulls are reconstructed too (Figure 40.6b) (Guo et al., 2016).

#### 40.4. TIME SERIES ANALYSIS: BOUNDARIES, MOTION, AND STRUCTURES

##### 40.4.1. Orientation and Motion of Boundaries (Minimum Residue Approach)

Most of the methods above utilize differences in timing between spacecraft to calculate orientations and velocities of a magnetospheric plasma structure. In addition to an underlying model of the structure to be studied, a minimum of four spacecraft is required to resolve the motion and orientation in full 3-D. An alternative, and often more flexible method, is the minimum residue method, in which minimization of measurements are performed. Although originally devised as single spacecraft methods, measurements from any number of spacecraft can be combined.

The simplest, and perhaps best known, residue method is probably minimum variance of the magnetic field (MVAB), in which the orientation minimizing  $div\mathbf{B}$  and  $d\mathbf{B}/dt$  are calculated. For a nearly 1-D structure (e.g. Harris like current sheets), this orientation is an estimate of the boundary normal. The first practical application of this technique was demonstrated in Sonnerup and Cahill (1967), using magnetic field measurements from a single spacecraft during a magnetopause crossing. Since the magnetic field is frame independent, motion of a structure cannot be derived from MVAB but will have to be derived from other measurements. A first attempt to determine both orientation and velocity of a structure was based on Faraday's law of magnetic flux conservation; it was presented in Terasawa et al. (1996). This method is now commonly referred to as Minimum Faraday Residue (MFR) and was cast into a least squares minimization scheme by Khrabrov and Sonnerup (1998).

With the availability of more accurate measurements of field and plasma moments, it became clear that various other conservation laws (mass conservation, flux conservation, charge conservation, etc.) could be applied in a similar way to estimate the orientation and motion of a plasma structure (Lepping and Argentiero, 1971; Vinas and Scudder, 1984; Kawano and Higuchi, 1996). Indeed, Sonnerup et al. (2006) formulated a generic approach to the use of conservation laws for orientation and motion, and demonstrated these using measurements from the Cluster satellites during magnetopause traversals. In this approach, known as Generic Minimum Residue Analysis, generic conservation laws are expressed as:

$$\frac{\delta}{\delta t}\eta_i + \frac{\delta}{\delta x_j}q_{ij} = 0 \quad (40.1)$$

where,  $\eta_i$  is the density component along the axis  $x_i$  ( $i = 1, 2, 3$ ) of the conserved quantity and  $q_{ij}$  is the transport tensor term. For example, conservation of charge, MVAJ (Haaland et al. (2004a), Xiao et al. (2004)), would be expressed as:

$$\frac{\delta}{\delta t}\rho_e + \nabla \cdot \vec{J} \quad (40.2)$$

where  $\rho_e$  is the charge density and  $\mathbf{J}$  is the current density, obtained either from the curlometer method described above, or from well calibrated plasma moments (Perri et al., 2017). Assuming a stationary structure with a constant motion,  $u_n$ , the time derivative in expression (40.1) can be transformed with a Galilean transformation to a spatial derivative and the expression expressed in the comoving frame as:

$$-u_n \frac{d}{dx'}\eta_i + \frac{d}{dx'}(n_j q_{ij}) = 0 \quad (40.3)$$

where  $x'$  is a coordinate in the comoving frame along the normal direction,  $\mathbf{n}$ . Integrating equation (40.3) gives:

$$-u_n \eta_i + n_j q_{ij} = C_i \quad (\text{where, } i = 1, 2, 3) \quad (40.4)$$

and  $C_i$  is a constant. Ideally, equation (40.4) should be satisfied for all  $\eta_i, q_{ij}$  pairs, but this is unlikely to hold for an ensemble of  $M$  samples by, e.g., a satellite traversing a plasma structure. In practice, one therefore usually defines a residue which is then minimized:

$$R = \frac{1}{M} \sum_{m=1}^M \left| -\eta_i^{(m)} u_n + n_j q_{ij}^{(m)} - C_i \right|^2 \quad (40.5)$$

where  $(m)$  indicates a single sample of the given quantity. The minimization of this residue, described in detail in Sonnerup et al. (2006), is a multistep process in which the optimal value  $C_i^*$  is determined first, then the optimal velocity vector,  $\mathbf{U}^*$ , and then finally the optimal value for the residue:

$$R^{**} = \mathbf{n}_i \mathbf{Q}_{ij} \mathbf{n}_j \quad (40.6)$$

where  $\mathbf{Q}_{ij}$  is a symmetric covariance matrix:

$$\mathbf{Q}_{ij} = \left\langle (\delta q_{ki} - U_i^* \delta \eta_k) (\delta q_{kj} - U_j^* \delta \eta_k) \right\rangle \quad (40.7)$$

Minimization of  $R^{**}$  implies finding a set of eigenvectors and eigenvalues from the covariance matrix  $\mathbf{Q}_{ij}$  and is identical to the procedure used in MVAB (where the transport terms vanish, and the covariance matrix ends up as  $\mathbf{Q}_{MVAB} = \langle \delta B_i \delta B_{ji} \rangle$ ). The eigenvector of  $\mathbf{Q}_{ij}$  corresponding to the smallest eigenvalue is an estimate of the normal vector,  $\mathbf{n}$ . We note that the covariance matrix in equation (40.7) is time independent. One can therefore

mix samples in random order from different spacecraft observations, add covariance matrices from several spacecraft or add covariance matrices from different methods, for example:

$$\begin{aligned} \text{QMV AB ALL} &= a \text{ QMV AB SC1} + b \text{ QMV AB SC2} \\ &+ c \text{ QMV AB SC3} + \dots \end{aligned} \quad (40.8)$$

$$\text{QMFR ALL} = a \text{ QMFR SC1} + b \text{ QMFR SC2} + \dots$$

$$\text{QTOT} = a \text{ QMV AB} + b \text{ QMFR} + \dots$$

where  $a$ ,  $b$ ,  $c$  can be normalizations according to, e.g., the individual eigenvalue ratios or a priori knowledge about particular result. Eigenvalues and eigenvectors are thereafter calculated from these combined covariance matrices. For velocities,  $\mathbf{U}^*$ , similar combinations can be made.

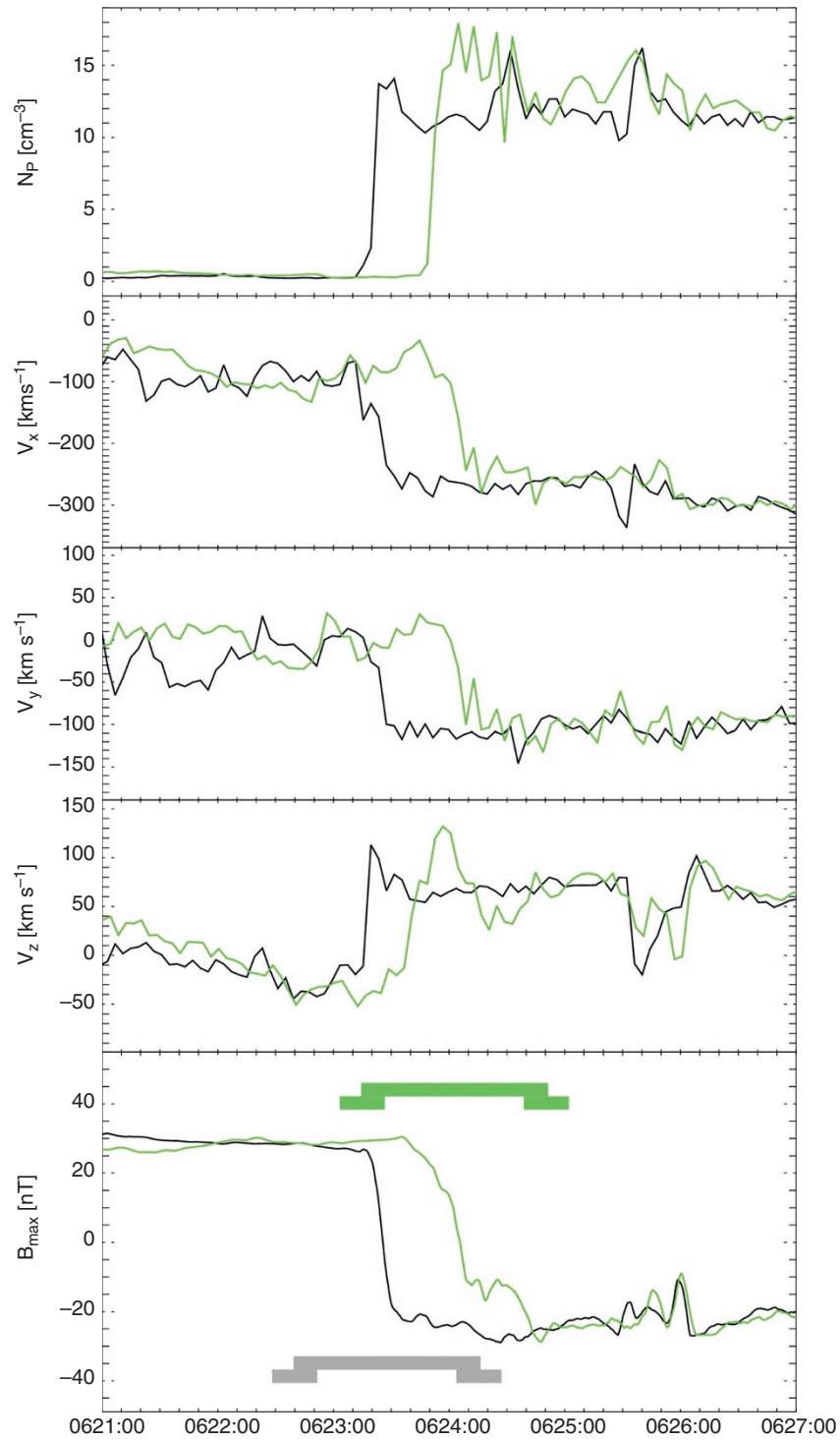
The above combination of methods or individual spacecraft work for an arbitrary number of spacecraft or methods provided that the underlying assumptions are satisfied. These assumptions, however, are usually not more stringent than those used for the timing or gradient methods above (e.g. planarity, stationarity, 1-D, linear variations between spacecraft). If measurements from more than one spacecraft are available, the above methods can also be combined with triangulation methods. This approach, now commonly referred to as the Discontinuity Analyzer (Dunlop and Woodward, 1998) has been applied in various forms on dual spacecraft configurations (Dunlop and Woodward, 1999), on three spacecraft (Horbury et al., 2001) and on four spacecraft constellations (Dunlop et al., 2002b; Haaland et al., 2004b).

Figure 40.7 (adapted from Sonnerup et al., 2006) shows measurements from two of the Cluster spacecraft during a dawn magnetopause crossing on 5 July 2001, around 0623 UT. The various minimum generic residue methods described above make use of combinations of these measurements to determine magnetopause orientation, motion and acceleration. For this event, the calculated motion was found to be very consistent between the various methods. Figure 40.8 illustrates the agreement in orientation between the different methods. Each symbol represent a normal orientation obtained from one of the above generic residue methods, here presented as an angular deviation from a common reference orientation. For both spacecraft, the orientations obtained from the methods utilizing plasma measurements agree to within  $6^\circ$ . The orientation obtained from the frequently used Minimum Variance of Magnetic field (MVAB) fails completely for Cluster 1 despite good eigenvalue ratios, and is approximately  $9^\circ$  off for Cluster 3.

#### 40.4.2. Dimensional and Spatiotemporal Analysis (MDD-STD)

**MDD method.** Using the measurements of a multispacecraft system with at least four spacecraft, all nine components of the magnetic gradient tensor  $\underline{G} = \nabla \underline{B}$  ( $\underline{B}$  can be replaced by any vector field, e.g.  $\underline{V}$  or  $\underline{E}$ ) at every observing moment can be estimated using various methods of estimation. Based on this, we can use a method called Minimum directional derivative (MDD) analysis (Shi et al., 2005, 2019) to determine the dimensionality (or dimension number) of the magnetic field and find the minimum and maximum gradient direction of the field, which can organize the data in a dimensionality-based coordinate system. Since this coordinate system is frequently used in theoretical works and simulations, the building of this coordinate can greatly help us interpret the data through some theoretical work or numerical simulations. The purpose of the MDD approach is seeking for the extremum of  $(\partial \bar{B} / \partial n)^2 = (\partial B_x / \partial n)^2 + (\partial B_y / \partial n)^2 + (\partial B_z / \partial n)^2$ , which is different to the MVA method, which is seeking for the extreme variation value of  $B_r^2$ . In the MDD analysis, if we find an eigenvalue equal to zero, it follows that  $(\partial \bar{B} / \partial n)^2 = (\partial B_x / \partial n)^2 + (\partial B_y / \partial n)^2 + (\partial B_z / \partial n)^2 = 0$ , which means the derivatives of  $B_x$ ,  $B_y$ , and  $B_z$  along this eigenvector direction  $\bar{n}$  should all be zero. This shows that the MDD method can provide a sufficient condition for one or two-dimensionality of a structure and then give the invariant axis directions at the same time.

Here we summarize the practical steps of dimension number determination and dim-based coordinate system setup, containing the following steps. First, estimate the field gradient tensor  $G = \nabla \underline{B}$  ( $\underline{B}$  can be  $\underline{V}$  or  $\underline{E}$ ) at every moment by multipoint measurements. Second, find the eigenvalues and eigenvectors of a symmetrical matrix  $L = GG^T = (\nabla \underline{B})(\nabla \underline{B})^T$ . The three eigenvalues  $\lambda_{\max}$ ,  $\lambda_{\text{mid}}$ , and  $\lambda_{\min}$  represent the maximum, intermediate and minimum values of the field directional derivatives, and the three eigenvectors  $\bar{n}_{\max}$ ,  $\bar{n}_{\text{mid}}$  and  $\bar{n}_{\min}$  represent the corresponding directions. Third, based on these calculations we conclude: (1) if  $\lambda_{\max}$ ,  $\lambda_{\text{mid}}$ , and  $\lambda_{\min}$  are similar to each other (i.e.  $\lambda_{\max}/\lambda_{\min}$ ,  $\lambda_{\max}/\lambda_{\text{mid}}$  ratios are small), it is a 3-D structure; (2) if  $\lambda_{\max}$ ,  $\lambda_{\text{mid}} \gg \lambda_{\min}$ , we can deem it as a quasi 2-D structure and its invariant direction is along  $\bar{n}_{\min}$ , i.e.,  $\partial/\partial n_{\min} = 0$ ; (3) if  $\lambda_{\max} \gg \lambda_{\text{mid}}$ ,  $\lambda_{\min}$ , we can regard it to be a quasi 1-D structure, and its invariant axes are any vectors in the plane of  $\bar{n}_{\text{mid}}$  and  $\bar{n}_{\min}$ , and the only variant direction (or its normal direction) is along  $\bar{n}_{\max}$ . Then the directions,  $\bar{n}_{\max}$ ,  $\bar{n}_{\text{mid}}$  and  $\bar{n}_{\min}$  are able to be used to build a dim-based coordinate system.



**Figure 40.7** Overview of measurements during a magnetopause encounter by Cluster 1 (black curves) and Cluster 3 (gray curves) on 5 July 2001, around 0624 UT. Starting at the top, the panels show: time series of measured ion density, temperature, three GSE velocity components, and the maximum variance magnetic field component. The analysis interval (25 samples) are indicated as horizontal bars in the lower panel.

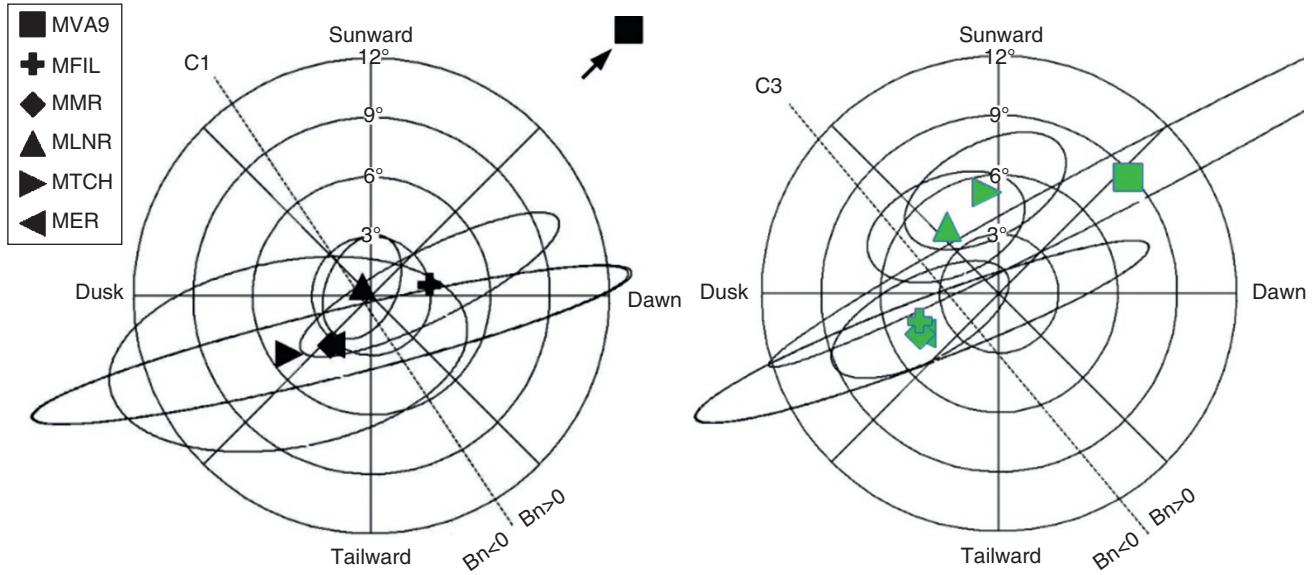


**Figure 40.8** Polar plots representing the orientation of magnetopause normal vectors for the event in Figure 40.7 for Cluster 1 (black symbols and curves) and Cluster 3 (gray). The center of each polar plot is a common reference orientation obtained from minimum variance of the magnetic field from all four Cluster spacecraft. Concentric circles labelled 3, 6, 9 degrees indicate the angular deviation from this reference orientation. Individual symbols represent normals obtained from the above methods, and the ellipses around them represent their statistical error bounds: MFR – Minimum Faraday Residue; MMR – Minimum Massflow Residue; MLMR – Minimum Linear Momentum Residue; MTER – Minimum Total Energy Residue; MER – Minimum Entropy Residue. The dashed line across the polar plot mark the  $B_n = 0$  planes (indicating a tangential discontinuity).

**STD Method.** When performing the deHoffmann–Teller (HT) analysis, we require the electric field to vanish in the frame we want to find, which is too strict because in some cases the electric field does not vanish but we only find the curl of electric field disappears in a proper frame where  $(\frac{\partial \vec{B}}{\partial t})_{str} = 0$ . In addition, Timing and MTA methods etc. assume the dimension number of a structure before performing the analysis. Trying to avoid these problems, Shi et al. (2006) developed a method of velocity calculation (or frame determination) for any structure dimension number, known as the “Spatiotemporal Difference” (STD) analysis of the magnetic field (see applications also in: Shi et al., 2009a, 2009b, 2013; Sun et al., 2010, 2012; Yao et al., 2016).

Here we summarize the practical steps needed to perform the STD analysis on actual data: First, the MDD analysis is carried out to obtain the dimensionality (dimension number) of the structure. Second, we solve the problem by a method depending on the structure dimension number. For a 3-D structure we can calculate three components of the velocity vector after estimating the magnetic gradient tensor  $G$  at every moment and the time variation of the magnetic field,  $\frac{\partial \vec{B}}{\partial t}|_{sc}$ . For a

2-D (1-D) structure, we can solve the equations

$$\frac{\partial \vec{B}}{\partial t}|_{sc} + \vec{V}_{str} \cdot \nabla \vec{B} = 0$$

(the first term on the left is the temporal variation caused by the motion through spatial gradients of the magnetic field, subscript “sc” means the calculation in the reference frame of the spacecraft, and

$\vec{V}_{str}$  (to be determined) is the velocity of the structure relative to the observer, that is, the spacecraft) in the original coordinate system (e.g., in GSE) and then project the velocity vector onto the eigenvectors calculated from the MDD method, or calculate the velocity along two (or one) directions, by solving equations

$$\frac{\partial \vec{B}}{\partial t}|_{sc, MDD} \cdot (\nabla \vec{B})^T|_{MDD} = -\vec{V}_{str}|_{MDD} \cdot \vec{\Lambda}$$

where the

subscript “MDD” means the calculations in the coordinate system determined by the eigenvectors of the MDD analysis,  $\vec{T}_r = \{ \vec{n}_1, \vec{n}_2, \vec{n}_3 \}$  (here “,” means different rows) is the transformation matrix from the original coordinate system (e.g., GSE) to the MDD eigenvector-based coordinate system,  $\vec{\Lambda} = \vec{T}_r^T (\nabla \vec{B}) (\nabla \vec{B})^T \vec{T}_r$  is a

diagonal matrix, of which the diagonal terms are the three eigenvalues  $\lambda_{\max}$ ,  $\lambda_{\text{mid}}$  and  $\lambda_{\min}$  from the MDD analysis, and  $\vec{V}_{str}|_{MDD} = \vec{V}_{str} \cdot \vec{T}_r$  is the velocity vector in the basis formed from eigenvectors. We emphasize here that the setting of time step length  $\Delta t$  is sometimes very important, and it should be set according to the characteristic length of the observed structure ( $\sim 1/10$  of the characteristic time scale of the structure). Finally, the velocity can be obtained along the normal direction for a 1-D structure or along the direction perpendicular to the invariant axis for a 2-D structure.

In Figure 40.9 we show an MDD and STD calculation using MMS data for a small-scale magnetosheath flux rope event in GSE coordinates (Yao et al., 2018; Shi et al., 2019, SSRs). From MDD calculation in Figure 40.9b, we find that the flux rope is 2-D, since  $\lambda_{\max}$ ,  $\lambda_{\text{mid}} \gg \lambda_{\min}$ . The flux rope axis is the invariant axis of this 2-D structure. The axis direction versus time is shown in Figure 40.9c. For this 2-D flux rope only two velocity components can be calculated, as shown in Figure 40.9d and Figure 40.9e, which can be combined to get its velocity perpendicular to the axis, i.e., velocity in the variant plane, as shown in Figure 40.9f. From the results we can see the velocity as a function of time, and then the acceleration can also be derived accordingly.

## 40.5. MULTISPACECRAFT WAVE VECTOR ANALYSIS TECHNIQUES

In this section, a brief introduction of the multispacecraft techniques performed in the Fourier domain, or more specifically, in the wave vector domain is given, as compared to single spacecraft techniques. Applications in the study of space plasma waves and turbulence are then enumerated and the drawbacks and improvements of the technique are discussed.

### 40.5.1. Fourier Domain Analysis

To understand the nature of the fluctuations in the wave vector domain, certain assumptions are needed when analyzing the time series data from a single spacecraft. One of these is the widely accepted Taylor “frozen-in flow” hypothesis, which connects the frequency and wave number projected in the flow direction:

$$\omega_{sc} \cong \mathbf{k} \cdot \mathbf{V} \quad (40.9)$$

where  $\omega_{sc}$  represent the frequency in the spacecraft frame,  $\mathbf{k}$  is the wave vector, and  $\mathbf{V}$  is the flow velocity. When the frequency of the fluctuations in the plasma frame is much smaller than the Doppler shift term  $\mathbf{k} \cdot \mathbf{V}$ , this hypothesis is supposed to be valid. For example, in the case of the solar wind, the flow speed could reach up to one order of

magnitude higher than the local Alfvén speed. Hence, most studies in the solar wind have assumed the validity of Taylor assumption, especially when interpreting the Kolmogorov-like power law spectrum at large scales (Chen, 2016, and references therein). Despite its simplicity, several fundamental properties of the fluctuations, including the wave vector  $\mathbf{k}$ , the wave frequency in the plasma rest frame, and other related parameters, are overlooked in the Taylor hypothesis. To overcome this shortcoming, advanced techniques utilizing observations from three-dimensional space are developed. Based on simultaneous four-point measurement, the k-filtering/wave telescope technique has been designed to estimate the distribution of energy in the frequency-wave vector domain (Pincon and Lefeuvre, 1991; Motschmann et al., 1996), so allowing the spatial properties of the fluctuations to be approached directly for the first time. Here we present only the basic principles of the technique; for more details of the derivation and other dispersion-based methods (i.e. Phase differencing in Balikhin et al., 1997), the reader is referred to Pincon and Glassmeier, 2008.

By assuming the decomposition of the fluctuations as a sum of plane waves with random phases, the fluctuation power in the frequency and wave vector domain can be determined from signals (i.e. magnetic field as shown below) from an array of four sensors:

$$P(\omega, \mathbf{k}_n) = \text{Tr} \left\{ \left( H^*(\mathbf{k}_n) M_B^{-1} H(\mathbf{k}_n) \right)^{-1} \right\} \quad (40.10)$$

where  $H(\mathbf{k}_n)$  contains the phase information of a wave at four spacecraft locations,  $M_B(\omega)$  is the cross-spectral density matrix of the magnetic field, which can be obtained from the expected value of the matrix product of  $\mathbf{B}(\omega)$  and its Hermitian adjoint  $\mathbf{B}^*(\omega)$ .  $\mathbf{B}(\omega)$  represents the Fourier transformation of the measured time series.

$$\mathbf{H}(\mathbf{k}_n) = \left( \mathbf{I} e^{i\mathbf{k}_n \cdot \mathbf{r}_1}, \mathbf{I} e^{i\mathbf{k}_n \cdot \mathbf{r}_2}, \mathbf{I} e^{i\mathbf{k}_n \cdot \mathbf{r}_3}, \mathbf{I} e^{i\mathbf{k}_n \cdot \mathbf{r}_4} \right)^T \quad (40.11)$$

$$\mathbf{M}_B(\omega) = E(\mathbf{B}(\omega) \mathbf{B}^*(\omega)) \quad (40.12)$$

$$\mathbf{B}(\omega) = \left( \mathbf{b}(\omega, \mathbf{r}_1), \mathbf{b}(\omega, \mathbf{r}_2), \mathbf{b}(\omega, \mathbf{r}_3), \mathbf{b}(\omega, \mathbf{r}_4) \right)^T \quad (40.13)$$

Note that when the stationarity of the fluctuations is satisfied (i.e. the mean field is almost constant), equation (40.4) can be approximated by an average of the matrix product  $M_B(\omega) = \sum_{l=1}^L \mathbf{B}(\omega) \mathbf{B}^*(\omega) / L$ .

In practice, the  $P(\omega, \mathbf{k}_n)$  estimation based on equation (40.3) can be improved by considering the solenoidality of the magnetic field as a constraint:

$$\hat{P}(\omega, \mathbf{k}_n) = \text{Tr} \left\{ \left( \mathbf{C}^*(\mathbf{k}_n) \mathbf{H}^*(\mathbf{k}_n) \mathbf{M}_B^{-1} \mathbf{H}(\mathbf{k}_n) \mathbf{C}(\mathbf{k}_n) \right)^{-1} \right\} \quad (40.14)$$

where  $\mathbf{C}(\mathbf{k}_n) = 1 + \mathbf{k}_n \mathbf{k}_n / k_n^2$  guarantees the solenoidality of the magnetic field.

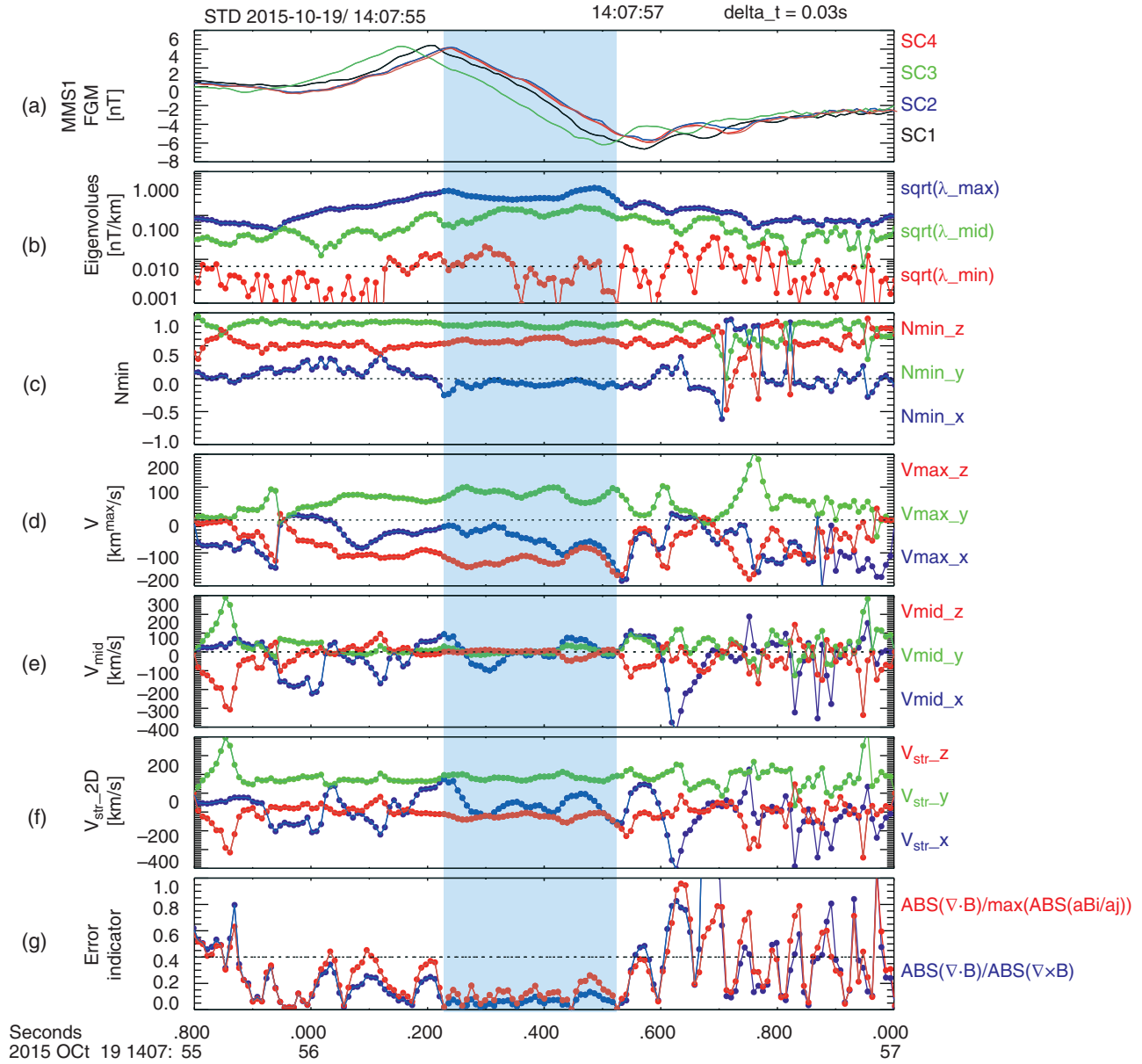


**Figure 40.9** STD analysis on a flux rope event (adapted from Shi et al., 2019, SSRs): (a) GSM  $B_x$  observed by MMS1-4 along the trajectory; (b) square root of eigenvalues  $\lambda_{\max}$ ,  $\lambda_{\text{mid}}$ , and  $\lambda_{\min}$  of the matrix  $L$  (dashed horizontal line indicates  $\delta B/l_{\max}$ , given measurement error  $\delta B = 0.05$  nT and the largest separation among spacecraft  $l_{\max}$ ); (c) minimum derivative direction  $\vec{n}_{\min}$ ; (d) velocity along the maximum derivative direction  $\vec{n}_{\max}$ ; (e) velocity along the intermediate derivative direction  $\vec{n}_{\text{mid}}$ ; (f) velocity of 2-D structure ( $V_{\max}$  and  $V_{\text{mid}}$  combined); (g) the calculation quality indicators calculated in two ways,  $\frac{|\nabla \cdot \vec{B}|}{|\nabla \times \vec{B}|}$  (blue line),  $\frac{|\nabla \cdot \vec{B}|}{\max(|\frac{\partial B_i}{\partial t_j}|)}$  ( $i, j = x/y/z$ ) (red line).

### 40.5.2. Applications

By applying the wave vector analysis technique to the electromagnetic field data from the Cluster mission, new properties of the waves/turbulence have been revealed in areas such as upstream of the bow shock (Narita et al., 2006; Constantinescu et al., 2007; Tjulin

et al., 2005), magnetosheath (Glassmeier et al., 2001; Sahraoui et al., 2006), cusp (Grison et al., 2005; Wang et al., 2014), magnetotail (Huang et al., 2010, 2012; Eastwood et al., 2009; Wang et al., 2016), and solar wind (Sahraoui et al., 2010b, Narita et al., 2011; Roberts et al., 2013; Perschke et al., 2013). Dispersion relations

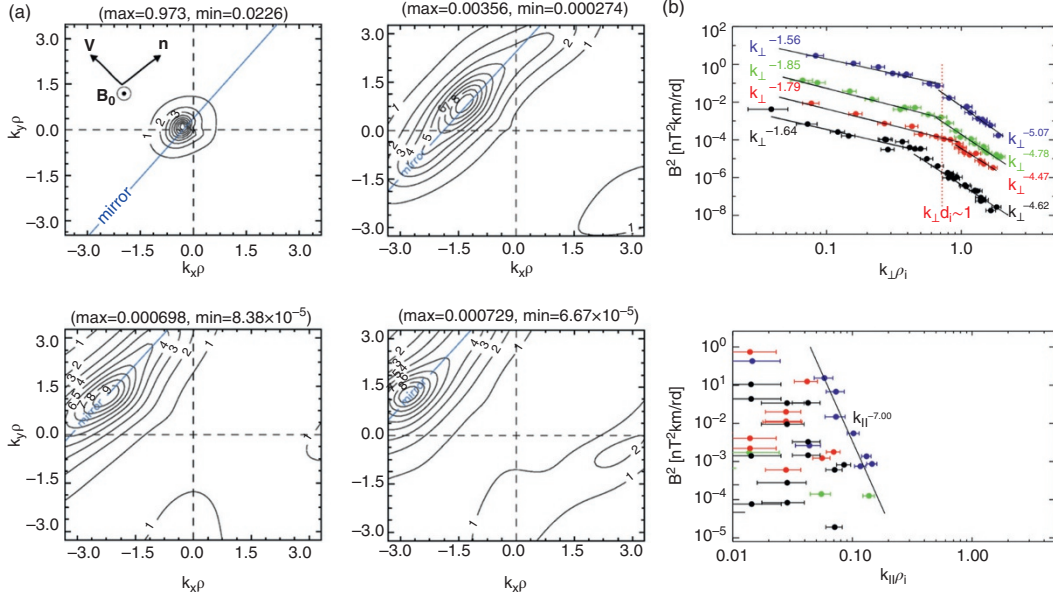


**Figure 40.10** (a) Identification of mirror mode structures, where the black contours represent the energy density  $P(\omega, \mathbf{k})$  and the blue lines denote the Doppler shift for static structures. (b) Anisotropic wave number spectra. Adapted from Sahraoui et al. (2006) and Sahraoui et al. (2010a).

and 3D wave vector spectra have been determined experimentally and compared with theoretical predictions, where most of the results show that turbulence is strongly anisotropic ( $\mathbf{k}_\perp \gg \mathbf{k}_\parallel$ ). For example, Figure 40.10a shows the static mirror structures at  $0.3 < k\rho_i < 3.5$  (Sahraoui et al., 2006), and Figure 40.10b presents the anisotropic wave number spectra at  $0.01 < k\rho_i < 2$  (Sahraoui et al., 2010b).

### 40.5.3. Extension of the Technique

Three limitations/drawbacks of the  $k$ -filtering technique, which require inspection with care (see the detailed discussion in Sahraoui et al. (2010a) and references therein), are identified here. (1) Spatial aliasing determines the available wave number range. Under the spacecraft separation  $d$ , the investigated  $k$  needs to be restricted to  $\sim(2\pi/100d, 2\pi/2d)$ ; note that the investigated frequency should also be restricted correspondingly. (2) A regular tetrahedral configuration is preferred for equal sampling of data in each spatial direction. (3) The waves with very close wavelengths are difficult to resolve. Moreover, the background noise of the  $k$  spectra may not be neglected in certain circumstances (Figure 40.11).

To address these problems, an extended analysis method named Multipoint Signal Resonator (MSR) has been proposed (Narita 2011, 2016a). The MSR method improves the signal-to-noise ratio of the solution by superposing a filter to the previous results:

$$\hat{P}_{msr}(\omega, \mathbf{k}_n) = \hat{P}(\omega, \mathbf{k}_n) * P_{EM} / \max(P_{EM}) \quad (40.15)$$

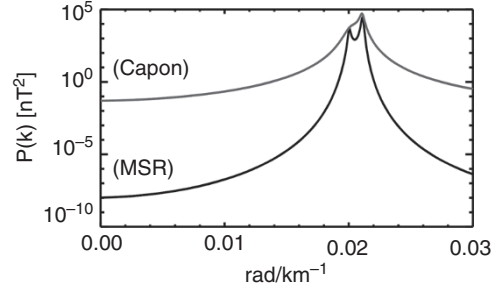


**Figure 40.11** Comparison of wave number spectra calculated from Capon and MSR method. Adapted from Narita et al., 2011).

where  $P_{EM} = \text{Tr}\{(C^*(\mathbf{k}_n)H^*(\mathbf{k}_n)G\Lambda^{-2}G^*H(\mathbf{k}_n)C(\mathbf{k}_n))^{-1}\}$ ,  $\mathbf{G} = (\mathbf{e}_1, \mathbf{e}_2, \dots, \mathbf{e}_{12})$ ,  $\Lambda^{-2} = \text{diag}\left(\left(\frac{\lambda_1}{\lambda_{12}}\right)^{-2}, \left(\frac{\lambda_2}{\lambda_{12}}\right)^{-2}, \dots, \left(\frac{\lambda_{12}}{\lambda_{12}}\right)^{-2}\right)$ ,  $\mathbf{e}_i$  and  $\lambda_i$  are the eigenvectors and eigenvalues of  $M_B$ .

The MSR method has been applied to density/magnetic field strength to understand the compressible fluctuations in the solar wind (Roberts et al., 2017). more recently, as seen in Figure 40.12, The dispersion relation diagram has been determined using observations from the magnetospheric multiscale (MMS) mission. finally, we note that, compared to the  $\sim 100$  KM resolution of cluster, the wavelength resolution for mms has been increased to  $\sim 10$  KM, which allows us to investigate electron scale fluctuations

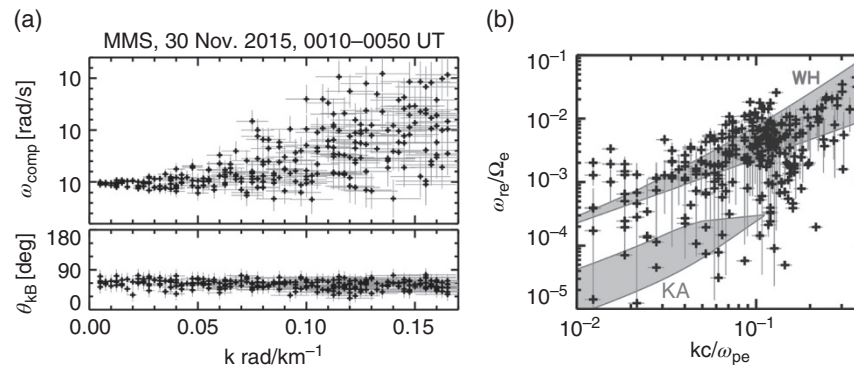


**Figure 40.12** (a) Dispersion relation diagram and wave vector direction distributions at ion-kinetic scales. (b) Dispersion relation diagram at electron-kinetic scales. Adapted from Narita et al., 2016a, 2016b.

(e.g., oblique whistler waves identified in Narita et al., 2016B).

#### 40.6. CONCLUSION

We have only been able to cover a limited set of applications, regions, and methods developed over the last two decades of closely spaced multipoint observations. Other applications have been covered elsewhere in this publication, however, as well as developments, in particular, to the smaller-scale regimes of the MMS mission. The purpose here has been to show where key applications of the methods have been carried out. Much of the description has focused on the manipulation of the four spacecraft magnetic field data, but with the advent of fast plasma measurements new associated methods are being developed (see Chapters 41 in this volume).

#### ACKNOWLEDGMENTS

This work is supported by NSFC grants 41574155 and 41431071, and by Natural Environment Research Council (NERC) Highlight Topic SWIGS grant (NE/P016863/1). MWD is partly supported by STFC in-house research grant (ST/M001083/1). MWD wishes to thank Ruilong Guo for provision of Figure 40.6 (b).

#### REFERENCES

- Angelopoulos, V. (2008), The THEMIS mission, *Space Sci. Rev.*, 141, 5–34, doi:10.1007/s11214-008-9336-1.
- Balikhin, M. A., T. Dudok de Wit, L. J. C. Woolliscroft, S. N. Walker, H. Alleyne, V. Krasnosel'skikh, et al. (1997), Experimental determination of the dispersion of waves observed upstream of a quasi-perpendicular shock, *Geophys. Res. Lett.*, 24, 787–790.
- Burch, J. L., T. E. Moore, R. B. Torbert, and B. L. Giles (2016), Magnetospheric Multiscale Overview and Science Objectives, *Space Sci. Rev.*, 5, 1–17, doi:10.1007/s11214-015-0164-9.
- Chanteur, G. (1998), Spatial Interpolation for four spacecraft: Theory. In G. Paschmann and P. Daly (Eds.), *Analysis methods for multispacecraft data, ISSI Science Report Series*, (Vol. 1, pp. 349–370). ESA Publications, Noordwijk, The Netherlands.
- Chen, C. H. K. (2016). Recent progress in astrophysical plasma turbulence from solar wind observations. *Journal of Plasma Physics*, 82(06), 535820602. <https://doi.org/10.1017/S0022377816001124>
- Chen, X. H., H. S. Fu, C. M. Liu, D. Cao, Z. Wang, M. W. Dunlop, et al. (2018a), Magnetic nulls in the reconnection driven by turbulence, *Astrophys. J.*, 852, 17, doi:10.3847/1538-4357/aa9991.
- Chen, Z. Z., H. S. Fu, T. Y. Wang, D. Cao, F. Z. Peng, J. Yang, and Y. Xu (2018b), Reconstructing the flux-rope topology using the FOTE method, *Sci. China Tech. Sci.*, 61, doi:10.1007/s11431-017-9201-1.
- Constantinescu, O. D., K.-H. Glassmeier, U. Motschmann, R. A. Treumann, K.-H. Fornacon, and M. Franz (2006), Plasma wave source location using CLUSTER as a spherical wave telescope, *J. Geophys. Res.*, 111, A09221, doi:10.1029/2005JA011550.
- De Keyser, J. (2008), Least-squares multi-spacecraft gradient calculation with automatic error estimation. *Ann. Geophys.*, 26, 3295–3316, <https://doi.org/10.5194/angeo-26-3295-2008>.
- De Keyser, J., F. Darrouzet, M. W. Dunlop, and P. M. E. Décréau (2007). Least-squares gradient calculation from multi-point observations of scalar and vector fields: Methodology and applications with Cluster in the plasmasphere, *Ann. Geophys.*, 25, 971–987, <https://doi.org/10.5194/angeo-25-971-2007>.
- Dong, X.-C., M. W. Dunlop, T.-Y. Wang, J.-B. Cao, K. J. Trattner, R. Bamford, et al. (2018), Carriers and sources of magnetopause current: MMS case study. *J. Geophys. Res.: Space Phys.*, 123, <https://doi.org/10.1029/2018JA025292>.
- Dunlop, M. W. and A. Balogh (2005), Magnetopause current as seen by Cluster, *Ann. Geophys.*, 23(3), 901–907, doi:10.5194/angeo-23-901-2005.
- Dunlop, M. W. and J. P. Eastwood (2008), The Curlometer and other gradient based methods. In G. Paschmann and P.W. Daly (Eds.), *Multi-spacecraft analysis methods revisited, ISSI Science Report Series* (Vol. 8, pp. 17–21). ESA Publications, Noordwijk, The Netherlands.

- Dunlop, M. W. and T. I. Woodward (1998), Discontinuity analysis: orientation and motion. In G. Paschmann and P. Daly (Eds.), *Analysis methods for multispacecraft data, ISSI Science Report Series*, (Vol. 1, pp. 271–306). ESA Publications, Noordwijk, The Netherlands.
- Dunlop, M. W., and T. I. Woodward (1999), Analysis of thick, non-planar boundaries using the discontinuity analyser, *Ann. Geophys.*, 17(8), 984–995.
- Dunlop, M. W., D. J. Southwood, K.-H. Glassmeier, and F. M. Neubauer (1988), Analysis of multipoint magnetometer data, *Adv. Space Res.*, 8, 273–277, doi:10.1016/0273-1177(88)90141-X.
- Dunlop, M. W., A. Balogh, K.-H. Glassmeier, and P. Robert (2002a), Four-point Cluster application of magnetic field analysis tools: The Curlometer, *J. Geophys. Res.*, 107(A11), 1384, doi:10.1029/2001JA005088.
- Dunlop, M. W., A. Balogh, P. Cargill, R. C. Elphic, K.-H. Fornacon, E. Georgescu, and F. Sedgemore-Schulthess (2002b), Cluster observes the Earth's magnetopause: Coordinated four-point magnetic field measurements, *Ann. Geophys.*, 19(10), 1449–1460.
- Dunlop, M. W., Q. H. Zhang, C. J. Xiao, J. S. He, Z. Y. Pu, R. C. Fear, et al. (2009), Reconnection at high latitudes: Antiparallel merging, *Phys. Rev. Lett.*, 102(7), 075005.
- Dunlop, M. W., Y.-Y. Yang, J.-Y. Yang, H. Lühr, C. Shen, N. Olsen, et al. (2015a), Multi-spacecraft current estimates at Swarm, *J. Geophys. Res.*, 120, doi:10.1002/2015JA021707.
- Dunlop, M. W., J.-Y. Yang, Y.-Y. Yang, C. Xiong, H. Lühr, Y. V. Bogdanova, et al. (2015b), Simultaneous field-aligned currents at Swarm and Cluster satellites, *Geophys. Res. Lett.*, 42, 3683–3691, doi:10.1002/2015GL063738.
- Dunlop, M. W., S. Haaland, C.P. Escoubet and X.-C. Dong (2016), Commentary on accessing 3-D currents in space: Experiences from Cluster, *J. Geophys. Res.*, 121, 7881–7886, doi:10.1002/2016JA022668.
- Dunlop, M. W., S. Haaland, X.-C. Dong, H. Middleton, P. Escoubet, Y.-Y. Yang, et al. (2018), Multi-point analysis of current structures and applications: Curlometer technique. In A. Keiling, O. Marghita, and M. Wheatland (Eds), *Electric currents in geospace and beyond, Geophysical Monograph Series* (Vol. 235, pp. 67–80). American Geophysical Union, doi:10.1002/9781119324522.ch4.
- Eastwood, J. P., A. Balogh, M. W. Dunlop, and C. W. Smith (2002), Cluster observations of the heliospheric current sheet and an associated magnetic flux rope and comparisons with ACE, *J. Geophys. Res.*, 107(A11), 1365, doi:10.1029/2001JA009158.
- Eastwood, J. P., T. D. Phan, S. D. Bale, and A. Tjulin (2009), Observations of turbulence generated by magnetic reconnection, *Phys. Rev. Lett.*, 102, 035001, doi:10.1103/PhysRevLett.102.035001.
- Escoubet, C. P., M. Fehringer, and M. Goldstein (2001), Introduction: the Cluster mission, *Ann. Geophys.*, 19, 1197–1200, doi:10.5194/angeo-19-1197-2001.
- Forsyth, C. et al. (2008), Observed tail current systems associated with bursty bulk flows and auroral streamers during a period of multiple substorms, *Ann. Geophys.*, 26, doi:10.5194/angeo-26-167-2008.
- Friis-Christensen, E., H. Lühr, D. Knudsen and R. Haugmans (2008), Swarm – An earth observation mission investigating geospace, *Adv. Space Res.*, 41, 210–216 doi:10.1016/j.asr.2006.10.008.
- Fu, H. S., A. Vaivads, Y. V. Khotyaintsev, V. Olshevsky, M. André, J. Cao, et al. (2015), How to find magnetic nulls and reconstruct field topology with MMS data?, *J. Geophys. Res.: Space Phys.*, 120, 3758–3782, doi:10.1002/2015ja021082.
- Fu, H. S., J. Cao, A. Vaivads, Y. V. Khotyaintsev, M. Andre, M. Dunlop, et al. (2016), Identifying magnetic reconnection events using the FOTE method, *J. Geophys. Res.: Space Phys.*, 121, 1263–1272, doi:10.1002/2015ja021701.
- Fu, H. S., A. Vaivads, Y. V. Khotyaintsev, M. André, J. B. Cao, V. Olshevsky, et al. (2017), Intermittent energy dissipation by turbulent reconnection, *Geophys. Res. Lett.*, 44, 37–43, doi:10.1002/2016GL071787.
- Fu, H. S., J. B. Cao, D. Cao, Z. Wang, A. Vaivads, Y. V. Khotyaintsev, et al. (2018), Evidence of magnetic nulls in electron diffusion region, *Geophys. Res. Lett.*, 46(1), 48–54.
- Fu, H. S., Z. Wang, Q. G. Zong, X. H. Chen, J. S. He, A. Vaivads, and V. Olshevsky (2020), Methods for finding magnetic nulls and reconstructing field topology: A review. In Q. Zong, P. Escoubet, D. Sibeck, G. Le, and H. Zhang (Eds.), *Dayside magnetosphere interactions, Geophysical Monograph Series* (Vol. 248, pp. 153–172). American Geophysical Union, Washington, DC.
- Glassmeier, K.-H., et al. (2001), Cluster as a wave telescope – First results from the fluxgate magnetometer, *Ann. Geophys.*, 19, 1439–1447.
- Greene, J. M. (1992), Locating three-dimensional roots by a bisection method, *J. Comput. Phys.*, 98, 194–198.
- Grison, B., F. Sahraoui, B. Lavraud, T. Chust, N. Cornilleau-Wehrlin, H. Rème, et al. (2005), Wave particle interactions in the high-altitude polar cusp: A Cluster case study, *Ann. Geophys.*, 23, 3699–3713.
- Guo, R., et al. (2013), Separator reconnection with antiparallel/component features observed in magnetotail plasmas, *J. Geophys. Res.: Space Phys.*, 118, 6116–6126, doi:10.1002/jgra.50569.
- Guo, R.-L., Z.-Y. Pu, L.-J. Chen, S.-Y. Fu, L. Xie, X.-G. Wang, et al. (2016), In-situ observations of flux ropes formed in association with a pair of spiral nulls in magnetotail plasmas, *Phys. Plasmas*, 23, 052901, https://doi.org/10.1063/1.4948415.
- Haaland, S., B. Ö. Sonnerup, M. Dunlop, E. Georgescu, G. Paschmann, B. Klecker, and A. Vaivads (2004a) Orientation and motion of a discontinuity from Cluster curlometer capability: Minimum variance of current density, *Geophys. Res. Letts.*, 31, L10804, doi:10.1029/2004GL020001.
- Haaland, S., B. Sonnerup, M. Dunlop, A. Balogh, E. Georgescu, H. Hasegawa, et al. (2004b), Four-spacecraft determination of magnetopause orientation, motion and thickness: comparison with results from single-spacecraft methods, *Ann. Geophys.*, 22(4), 1347–1365.
- Hamrin, M., K. Rönmark, N. Börlin, and A. Vaivads (2008), GALS: Rradient Analysis by Least Squares. *Ann. Geophys.*, 26, 3491–3499, https://doi.org/10.5194/angeo-26-3491-2008.

- Harris, M. J. (1962), On a plasma sheet separating regions of oppositely directed magnetic field, *Nuovo Cimento*, 23, 115–121.
- Harvey, C. C. (1998), Spatial gradients and the volumetric tensor. G. Paschmann and P. Daly (Eds.), *Analysis methods for multi-spacecraft data, ISSI Science Report Series*, (Vol. 1, pp. 307–322). ESA Publications, Noordwijk, The Netherlands.
- He, J.-S., et al. (2008a), A magnetic null geometry reconstructed from Cluster spacecraft observations, *J. Geophys. Res.*, 113, A05205, doi:10.1029/2007JA012609.
- He, J.-S., et al. (2008b), Electron trapping around a magnetic null, *Geophys. Res. Lett.*, 35, L14104, doi:10.1029/2008GL034085.
- Horbury, T. S., D. Burgess, M. Fraenz, and C. J. Owen (2001), Three spacecraft observations of solar wind discontinuities, *Geophys. Res. Lett.*, 28(4), 677–680.
- Huang, S. Y., et al. (2018), Observations of the Electron Jet Generated by Secondary Reconnection in the Terrestrial Magnetotail, *Astrophys. J.*, 862, 144, doi:10.3847/1538-4357/aacd4c
- Huang, S. Y., M. Zhou, F. Sahraoui, X. H. Deng, Y. Pang, Z. G. Yuan, et al. (2010), Wave properties in the magnetic reconnection diffusion region with high  $\beta$ : Application of the k-filtering method to Cluster multispacecraft data, *J. Geophys. Res.*, 115, A12211, doi:10.1029/2010JA015335.
- Huang, S. Y., et al. (2012), Observations of turbulence within reconnection jet in the presence of guide field, *Geophys. Res. Lett.*, 39, L11104, doi:10.1029/2012GL052210.
- Kawano, H., and T. Higuchi (1996), A generalization of the minimum variance method, *Ann. Geophys.*, 14, 1019.
- Khrabrov, A. V., and B. U. Ö. Sonnerup (1998), Orientation and motion of current layers: minimization of the Faraday residue, *Geophys. Res. Lett.*, 25, 2373.
- Lau, Y. T., and J. M. Finn (1990), Three-dimensional kinematic reconnection in the presence of field nulls and closed field lines, *Astrophys. J.*, 350, 672–691.
- Lavraud, B., et al. (2016), Currents and associated electron scattering and bouncing near the diffusion region at Earth's magnetopause, *Geophys. Res. Lett.*, 43, 3042–3050, doi:10.1002/2016GL068359.
- Lepping, R. P., and Argentiero, P. D. (1971), Single spacecraft method of estimating shock normals, *J. Geophys. Res.*, 76(19), 4349–4359. <https://doi.org/10.1029/ja076i019p04349>.
- Liu, C. M., H. S. Fu, D. Cao, Y. Xu, and A. Divin (2018), Detection of magnetic nulls around reconnection fronts, *Astrophys. J.*, 860, 128, doi:10.3847/1538-4357/aac496.
- Liu, C. M., Z. Z. Chen, Z. Wang, and Y. Y. Liu (2019), Evidence of radial nulls near reconnection fronts, *Astrophys. J.*, 871(2), 209.
- Man, H. Y. et al. (2018), In situ observation of magnetic reconnection between an earthward propagating flux rope and the geomagnetic field. *Geophys. Res. Lett.*, 45, 8729–8737, <https://doi.org/10.1029/2018GL079778>,
- Marchaudon, A., J.-C. Cerisier, M. W. Dunlop, F. Pitout, J.-M. Bosqued, and A. N. Fazakerley (2009), Shape, size, velocity and field-aligned currents of dayside plasma injections: a multi-altitude study, *Ann. Geophys.*, 27, 1251–1266, doi:10.5194/angeo-27-1251-2009.
- Middleton, H. R. and A. Masson (2016), The Curlometer Technique: a beginner's guide. ESA Technical Note ESDC-CSA\_TN\_0001, <http://www.cosmos.esa.int/web/csa/multi-spacecraft>.
- Motschmann, U., T. I. Woodward, K.-H. Glassmeier, D. J. Southwood, and J.-L. Pinçon (1996), Wavelength and directional filtering by magnetic measurements at satellite arrays: Generalized minimum variance analysis, *J. Geophys. Res.*, 101, 4961.
- Nakamura, R., W. Baumjohann, M. Fujimoto, Y. Asano, A. Runov, C. Owen, et al. (2008), Cluster observations of an ion-scale current sheet in the magnetotail under the presence of a guide field, *J. Geophys. Res.*, 113(A7), doi:10.1029/2007JA012760.
- Narita, Y., K.-H. Glassmeier, and R. A. Treumann (2006), Wave-number spectra and intermittency in the terrestrial foreshock region, *Phys. Rev. Lett.*, 97, 191101, doi:10.1103/PhysRevLett.97.191101.
- Narita, Y., S. P. Gary, S. Saito, K.-H. Glassmeier, and U. Motschmann (2011), Dispersion relation analysis of solar wind turbulence, *Geophys. Res. Lett.*, 38, L05101, doi:10.1029/2010GL046588.
- Narita, Y., R. Nakamura, and W. Baumjohann (2013), Cluster as current sheet surveyor in the magnetotail, *Ann. Geophys.*, 31, 1605–1610, doi:10.5194/angeo-31-1605-2013.
- Narita, Y., et al. (2016a), Wave telescope technique for MMS magnetometer, *Geophys. Res. Lett.*, 43, 4774–4780, doi:10.1002/2016GL069035.
- Narita, Y., et al. (2016b), On electron-scale whistler turbulence in the solar wind, *Astrophys. J. Lett.*, 827, L8, doi:10.3847/2041-8205/827/1/L8.
- Panov, E., J. Büchner, M. Fränz, A. Korth, Y. Khotyaintsev, B. Nikutowski, et al. (2006), CLUSTER spacecraft observation of a thin current sheet at the Earth's magnetopause, *Adv. Space Res.*, 37(7), 1363–1372, doi:10.1029/2006GL026556.
- Parnell, C. E., J. M. Smith, T. Neukirch, and E. R. Priest (1996), The structure of three-dimensional magnetic neutral points, *Phys. Plasmas*, 3, 759–770, doi:10.1063/1.871810.
- Paschmann, G., and P. W. Daly (Eds.) (1998), *Analysis methods for multispacecraft data, ISSI Science Report Series*, (Vol. 1). ESA Publications, Noordwijk,
- Paschmann, G., and P. W. Daly (Eds.) (2008), *Multi-spacecraft analysis methods revisited, ISSI Science Report Series* (Vol. 8). ESA Publications, Noordwijk, The Netherlands.
- Perri, S., Valentini, F., Sorriso-Valvo, L., Reda, A., and Malara, F. (2017), On the estimation of the current density in space plasmas: Multi- versus single-point techniques. *Planet. Space Sci.*, 140(1), 6–10, <https://doi.org/10.1016/j.pss.2017.03.008>.
- Perschke, C., Y. Narita, S. P. Gary, U. Motschmann, and K.-H. Glassmeier (2013), Dispersion relation analysis of turbulent magnetic field fluctuations in fast solar wind, *Ann. Geophys.*, 31, 1949.
- Pinçon, J.-L., and K.-H. Glassmeier (2008), Multi-spacecraft methods of wave field characterization. In G. Paschmann and P.W. Daly (Eds.), *Multi-spacecraft analysis methods revisited, ISSI Science Report Series* (Vol.8, pp. 47–54). ESA Publications, Noordwijk, The Netherlands.

- Pinçon, J. L., and F. Lefeuvre (1991), Local characterization of homogeneous turbulence in a space plasma from simultaneous measurements of field components at several points in space, *J. Geophys. Res.*, 96, 1789–1802.
- Priest, E. R., and V. S. Titov (1996), Magnetic reconnection at three-dimensional null points, *Phil. Trans. R. Soc., A*, 354, 2951–2992.
- Ritter, P., H. Lühr, and J. Rauberg (2013), Determining field-aligned currents with the Swarm constellation mission, *Earth Planets Space*, 65, 1285–1294, doi:10.5047/eps.2013.09.006.
- Robert, P., M. W. Dunlop, A. Roux, and G. Chanteur (1998), Accuracy of current density determination. In G. Paschmann and P. Daly (Eds.), *Analysis methods for multispacecraft data, ISSI Science Report Series*, (Vol. 1, pp. 395–418). ESA Publications, Noordwijk, The Netherlands.
- Roberts, O. W., X. Li, and B. Li (2013), Kinetic plasma turbulence in the fast solar wind measured by Cluster, *Astrophys. J.*, 769, 58, doi:10.1088/0004-637X/769/1/58.
- Roberts, O. W., Y. Narita, X. Li, C. P. Escoubet, and H. Laakso (2017), Multipoint analysis of compressive fluctuations in the fast and slow solar wind, *J. Geophys. Res.: Space Phys.*, 122, 6940–6963, doi:10.1002/2016JA023552.
- Rong, Z. J., W. X. Wan, C. Shen, X. Li, M. W. Dunlop, A. A. Petrukovich, et al. (2011), Statistical survey on the magnetic structure in magnetotail current sheets, *J. Geophys. Res.*, 116, A09218, doi:10.1029/2011JA016489.
- Roux, A., P. Robert, D. Fontaine, O. LeContel, P. Canu, and P. Louarn (2015), What is the nature of magnetosheath FTEs? *J. Geophys. Res.*, 120(6), 4576–4595, doi:10.1002/2015JA020983.
- Runov et al. (2006), Local structure of the magnetotail current sheet: 2001 Cluster observations, *Ann. Geophys.*, 24, 247–262, doi:10.5194/angeo-24-247-2006.
- Russell, C T, J G Luhmann, and R J Strangeway (2016). *Space physics: An introduction*. Cambridge University Press.
- Sahraoui, F., G. Belmont, L. Rezeau, N. Cornilleau-Wehrin, J. L. Pinçon, and A. Balogh (2006), Anisotropic turbulent spectra in the terrestrial magnetosheath as seen by the Cluster spacecraft, *Phys. Rev. Lett.*, 96, 075002, doi:10.1103/PhysRevLett.96.075002.
- Sahraoui, F., G. Belmont, M. L. Goldstein, and L. Rezeau (2010a), Limitations of multi spacecraft data techniques in measuring wave number spectra of space plasma turbulence, *J. Geophys. Res.*, 115, A04206, doi:10.1029/2009JA014724.
- Sahraoui, F., M. L. Goldstein, G. Belmont, P. Canu, and L. Rezeau (2010b), Three dimensional anisotropic k spectra of turbulence at subproton scales in the solar wind, *Phys. Rev. Lett.*, 105, 131101
- Shen, C., and M. W. Dunlop (2008), Geometric structure analysis of the magnetic field. In G. Paschmann and P.W. Daly (Eds.), *Multi-spacecraft analysis methods revisited, ISSI Science Report Series* (Vol. 8, pp. 27–32). ESA Publications, Noordwijk, The Netherlands.
- Shen, C., X. Li, M. Dunlop, Z. X. Liu, A. Balogh, D. N. Baker, et al. (2003), Analyses on the geometrical structure of magnetic field in the current sheet based on cluster measurements, *J. Geophys. Res.*, 108(A5), 1168, doi:10.1029/2002JA009612.
- Shen, C., X. Li, M. Dunlop, Q. Q. Shi, Z. X. Liu, E. Lucek, and Z. Q. Chen (2007), Magnetic field rotation analysis and the applications, *J. Geophys. Res.*, 112, A06211, doi:10.1029/2005JA011584.
- Shen, C. et al. (2008a), Flattened current sheet and its evolution in substorms. *J. Geophys. Res.*, 113, A07S21, doi:10.1029/2007JA012812.
- Shen, C., Z. J. Rong, X. Li, M. Dunlop, Z. X. Liu, H. V. Malova, et al. (2008b), Magnetic configurations of the tilted current sheets in magnetotail, *Ann. Geophys.*, 26(11), 3525–3543.
- Shen, C., et al. (2011), The magnetic configuration of the high-latitude cusp and dayside magnetopause under strong magnetic shears, *J. Geophys. Res.*, 116, A09228, doi:10.1029/2011JA016501.
- Shen, C., J. Rong, M. Dunlop, Y. H. Ma, G. Zeng and Z. X. Liu (2012), Spatial gradients from irregular, multiple-point spacecraft configurations, *J. Geophys. Res.*, 117, A11207, doi:10.1029/2012JA018075.
- Shen, C., et al. (2014), Direct calculation of the ring current distribution and magnetic structure seen by Cluster during geomagnetic storms, *J. Geophys. Res.*, 119, 2458–2465, doi:10.1002/2013JA019460.
- Shi, J.-K. et al. (2010), South-north asymmetry of field-aligned currents in the magnetotail observed by Cluster, *J. Geophys. Res.*, 115, doi:10.1029/2009JA014446.
- Shi, Q. Q., C. Shen, Z. Y. Pu, M. W. Dunlop, Q.-G. Zong, H. Zhang, et al. (2005), Dimensional analysis of observed structures using multipoint magnetic field measurements: Application to Cluster, *Geophys. Res. Lett.*, 32, L12105, doi:10.1029/2005GL022454.
- Shi, Q. Q., C. Shen, M. W. Dunlop, Z. Y. Pu, Q.-G. Zong, Z. X. Liu, et al. (2006), Motion of observed structures calculated from multi-point magnetic field measurements: Application to Cluster, *Geophys. Res. Lett.*, 33, L08109, doi:10.1029/2005GL025073.
- Shi, Q. Q., Q.-G. Zong, H. Zhang, Z. Y. Pu, S.Y. Fu, L. Xie, et al. (2009a), Cluster observations of the entry layer equatorward of the cusp under northward interplanetary magnetic field, *J. Geophys. Res.*, 114, A12219, doi:10.1029/2009JA014475.
- Shi, Q. Q., Z. Y. Pu, J. Soucek, Q.-G. Zong, S. Y. Fu, L. Xie, et al. (2009b), Spatial structures of magnetic depression in the Earth's high-altitude cusp: Cluster multipoint observations, *J. Geophys. Res.*, 114, A10202, doi:10.1029/2009JA014283.
- Shi, Q. Q., Q.-G. Zong, S.Y. Fu, M.W. Dunlop, Z.Y. Pu, G.K. Parks, et al. (2013), Solar wind entry into the high-latitude terrestrial magnetosphere during geomagnetically quiet times, *Nat. Commun.*, 4, 1466, doi:10.1038/ncomms2476.
- Shi, Q. Q., A. M. Tian, S. C. Bai, H. Hasegawa, A. W. Degeling, Z. Y. Pu, et al. (2019), Dimensionality, coordinate system and reference frame for analysis of in-situ space plasma and field data. *Space Sci. Rev.*, 215, 35, <https://doi.org/10.1007/s11214-019-0601-2>.
- Sonnerup, B. U. Ö., and L. J. Cahill (1967), Magnetopause structure and attitude from Explorer 12 observations. *J. Geophys. Res.*, 72, 171–183, <https://doi.org/10.1029/JZ072i001p00171a>.
- Sonnerup, B. U. Ö., H. Hasegawa, W.-L. Teh, and L.-N. Hau (2006), Grad-Shafranov reconstruction: an overview, *J. Geophys. Res.*, 111(A9), <https://doi.org/10.1029/2006JA011717>.

- Sun W. J., Q. Q. Shi, S. Y. Fu, Q.-G. Zong, Z. Y. Pu, L. Xie, et al. (2010), Statistical research on the motion properties of the magnetotail current sheet: Cluster observations, *Sci. China: Technol. Sci.*, 53, 1732–1738, doi:10.1007/s11431-010-3153-y.
- Sun, W. J., Q. Q. Shi, S. Y. Fu, Z. Y. Pu, M. W. Dunlop, A. P. Walsh, et al. (2012), Cluster and TC-1 observation of magnetic holes in the plasma sheet, *Ann. Geophys.*, 30, 583–595, doi:10.5194/angeo-30-583-2012, 2012.
- Terasawa, T., H. Kawano, I. Shinohara, T. Mukai, Y. Saito, M. Hoshino, et al. (1996), On the determination of a moving MHD structure: minimization of the residue of integrated Faraday's equation, *J. Geomagn. Geoelectr.*, 48(5–6), 603–614.
- Tjulin, A., J. L. Pinçon, and F. Sahraoui (2005), The k-filtering technique applied to wave electric and magnetic field measurements from the Cluster satellites, *J. Geophys. Res.*, 110, A11224, doi:10.1029/2005JA011125.
- Vallat, C., et al. (2005), First current density measurements in the ring current region using simultaneous multi-spacecraft CLUSTER-FGM data, *Ann. Geophys.*, 23, 1849–1865, doi:10.5194/angeo-23-1849-2005.
- Viñas, A. F., and Scudder, J. D. (1984), Fast and optimal solution to the 'Rankine-Hugoniot problem'. *J. Geophys. Res.*, 91, 39–58.
- Vogt, J., G. Paschmann, and G. Chanteur (2008), Reciprocal vectors. In G. Paschmann and P.W. Daly (Eds.), *Multi-spacecraft analysis methods revisited, ISSI Science Report Series* (Vol. 8, pp. 27–30). ESA Publications, Noordwijk, The Netherlands.
- Vogt, J., A. Albert, and O. Marghitsu (2009), Analysis of three-spacecraft data using planar reciprocal vectors: Methodological framework and spatial gradient estimation, *Ann. Geophys.*, 27, 3249–3273, doi:10.5194/angeo-27-3249-2009.
- Vogt, J., E. Sorbalo, M. He, and A. Blagau (2013), Gradient estimation using configurations of two or three spacecraft, *Ann. Geophys.*, 31, 1913–1927, <http://www.ann-geophys.net/31/1913/2013/>.
- Wang, J., J. Cao, H. Fu, W. Liu, and S. Lu (2017), Enhancement of oxygen in the magnetic island associated with dipolarization fronts, *J. Geophys. Res.: Space Phys.*, 122, 185–193, doi:10.1002/2016ja023019.
- Wang, T., J.-B. Cao, H. Fu, W. Liu, and M. Dunlop (2014), Turbulence in the Earth's cusp region: The k-filtering analysis, *J. Geophys. Res.: Space Phys.*, 119, 9527–9542, doi:10.1002/2014JA019997.
- Wang, T., J. Cao, H. Fu, X. Meng, and M. Dunlop (2016), Compressible turbulence with slow-mode waves observed in the bursty bulk flow of plasma sheet, *Geophys. Res. Lett.*, 43, 1854–1861, doi:10.1002/2016GL068147.
- Wang, X., and A. Bhattacharjee (1996), A three-dimensional reconnection model of the magnetosphere: Geometry and kinematics, *J. Geophys. Res.*, 101, 2641–2653.
- Xiao, C. J., Z. Y. Pu, Z. W. Ma, S. Y. Fu, Z. Y. Huang, and Q.-G. Zong (2004), Inferring of flux rope orientation with the minimum variance analysis technique. *J. Geophys. Res.*, 109, A11218. <https://doi.org/10.1029/2004JA010594>.
- Xiao, C. J., et al. (2006), In situ evidence for the structure of the magnetic null in a 3D reconnection event in the Earth's magnetotail, *Nat. Phys.*, 2, 478–483, doi:10.1038/nphys342.
- Xiao, C. J., et al. (2007), Satellite observations of separator-line geometry of three-dimensional magnetic reconnection, *Nat. Phys.*, 3, 609–613.
- Xiao, C., Liu, W., Shen, C., Zhang, H., and Rong, Z. (2018), Study on the curvature and gradient of the magnetic field in Earth's cusp region based on the magnetic curvature analysis method. *J. Geophys. Res.: Space Phys.*, 123, <https://doi.org/10.1029/2017JA025028>.
- Yang, Y. Y., C. Shen, Y. C. Zhang, Z. J. Rong, X. Li, M. Dunlop, et al. (2014), The force-free configuration of flux ropes in geomagnetotail: Cluster observations, *J. Geophys. Res.: Space Phys.*, 119, 6327–6341, doi:10.1002/2013JA019642.
- Yang, Y.-Y., C. Shen, M. Dunlop, Z.-J. Rong, X. Li, V. Angelopoulos, et al. (2016), Storm time current distribution in the inner magnetospheric equator: THEMIS observations, *J. Geophys. Res.*, 120, doi:10.1002/2015JA022145.
- Yao, S. T., Q. Q. Shi, Z. Y. Li, X. G. Wang, A. M. Tian, W. J. Sun, et al. (2016), Propagation of small size magnetic holes in the magnetospheric plasma sheet, *J. Geophys. Res.: Space Phys.*, 121, 5510–5519, doi:10.1002/2016JA022741.
- Yao, S. T., Q. Q. Shi, R. L. Guo, Z. H. Yao, A. M. Tian, A. W. Degeling, et al. (2018), Magnetospheric multiscale observations of electron scale magnetic peak, *Geophys. Res. Lett.*, 45(2), 527–537, <https://doi.org/10.1002/2017gl075711>.
- Zhang, Q.-H., M. W. Dunlop, M. Lockwood, R. Holme, Y. Kamide, W. Baumjohann, et al. (2011), The distribution of the ring current: Cluster observations, *Ann. Geo.*, 29, 1655–1662, doi:10.5194/angeo-29-1655-2011.
- Zhang, Y. C., et al. (2013), Two different types of plasmoids in the plasma sheet: Cluster multisatellite analysis application, *J. Geophys. Res.: Space Phys.*, 118, 5437–5444, doi:10.1002/jgra.50542.
- Zhang, Y. C., et al. (2016), First in situ evidence of electron pitch angle scattering due to magnetic field line curvature in the ion diffusion region, *J. Geophys. Res.: Space Phys.*, 121, doi:10.1002/2016JA022409.